Available online at www.sciencedirect.com
ScienceDirect
Comput. Methods Appl. Mech. Engrg. xxx (xxxx) xxx
Computer methods in applied mechanics and engineering
www.elsevier.com/locate/cma

Highlights

An electromechanical micropolar peridynamic model

Comput. Methods Appl. Mech. Engrg. xxx (xxxx) xxx

Vito Diana*, Valter Carvelli

- An implicit electro-mechanical peridynamic formulation for isotropic solids is proposed.
- The model includes a microelectrical energy function and a microelastic energy function.
- The electro-mechanical micropolar peridynamic model can consider variable Poisson's ratio.
- The model was validated by analytical solutions, FEM and experiments.
- The electro-mechanical predictions involve fracture and piezoresistive behavior.

Please cite this article as: V. Diana and V. Carvelli, An electromechanical micropolar peridynamic model, Computer Methods in Applied Mechanics and Engineering (2020) 112998, https://doi.org/10.1016/j.cma.2020.112998.

CMA: 112998

ARTICLE IN PRESS

Available online at www.sciencedirect.com

ScienceDirect

Comput. Methods Appl. Mech. Engrg. xxx (xxxx) xxx

Computer methods in applied mechanics and engineering

www.elsevier.com/locate/cma

An electromechanical micropolar peridynamic model

Vito Diana*, Valter Carvelli

Department ABC, Politecnico di Milano, Piazza Leonardo da Vinci 32, Milano, 20133, Italy

Received 16 January 2020; received in revised form 12 March 2020; accepted 13 March 2020
Available online xxxx

Abstract

A micropolar peridynamic model for in-plane electro-mechanical behavior of isotropic solids is presented in this paper. The conceived analytical implicit formulation of the electrical part of the model is based on the definition of a proper microelectrical energy function and a specific bond electrical field measure. A compatibility condition and a constitutive relationship have been derived and thus the electrical stiffness operator has been obtained. The electrical formulation is then coupled with a mechanical micropolar peridynamic formulation with adjustable Poisson's ratio. The obtained unified model is capable to predict the elastic response and the electrical conduction of elastic brittle materials taking into account the influence of cracks and other defects. The accuracy of the proposed model has been assessed by several problems including the simulation of fracture propagation and damage sensing in a lamina under tensile loading and the piezoresistive response of nanocomposite materials.

Keywords: Peridynamics; Electrical conduction; Micropolar; Fracture; Damage sensing

1. Introduction

Peridynamics is a non-local theory of mechanics [1] which recasts the balance laws as integral equations instead of the typical partial differential equations of classical local continuum mechanics. The peridynamics (PD) equations are considered strongly non-local as opposed to a weak non-locality or a strain gradient type non-locality [2]. The internal force density is represented as an integral of forces between material particles as opposed to an integral of stress in a weak non-local theory [3,4] or as a divergence of stress in classical continuum theories [5,6]. Moreover, being the displacement the primary kinematic field variable used in constitutive equations, all continuity requirements on the displacement field are removed [6].

The originally proposed theory, referred to as bond-based PD (BBPD), is a central force model. Therefore, as in the rari-constant theory [7–9], Poisson's ratio is restricted to $\nu = 1/4$ for three-dimensional (3D) and plane strain, and $\nu = 1/3$ for plane stress. To overcome this shortcoming, Silling et al. [10] introduced a more general formulation, coined state-based PD (SBPD) in which the pairwise force between two particles depends on the deformations of all nodes within their neighborhood. Other efforts along these lines include the non-ordinary state-based model (NOSB) [11,12], the conjugated bond-pair-based PD formulation [13,14], and the Gerstle's non-local lattice beam model [15,16]. Recently, a generalized micropolar model for isotropic and orthotropic materials, inspired by Voigt's studies on crystals [17], has also been presented [18,19].

* Corresponding author.
E-mail address: vito.diana@polimi.it (V. Diana).

https://doi.org/10.1016/j.cma.2020.112998
0045-7825/

Please cite this article as: V. Diana and V. Carvelli, An electromechanical micropolar peridynamic model, Computer Methods in Applied Mechanics and Engineering (2020) 112998, https://doi.org/10.1016/j.cma.2020.112998.

PD theory has been applied extensively to problems involving fracture [2,20–23], plasticity and viscoelasticy [24–27].

The universal nature of partial differential equations allows Peridynamics to be considered as general nonlocal continuum theory, and thus to be extended also to other physical fields. In fact, the integral equations of peridynamics have been applied by Gerstle et al. [28] to the study of one-dimensional electromigration, by using a framework which allows four coupled physical processes to be modeled simultaneously: mechanical deformation, heat transfer, electrical potential distribution, and vacancy diffusion. Bobaru and Duangpanya proposed a one dimensional peridynamic heat conduction equation, and solved the 2D peridynamic transient heat conduction problem in bodies with evolving discontinuities following a bond-based approach [29,30] and using a direct implementation of the peridynamic balance equations. A formal derivation for a state-based peridynamic model of heat diffusion was presented by Oterkus et al. [31]. The same authors proposed later a coupled peridynamic thermo-mechanic model starting from thermodynamic considerations [32], and using explicit schemes to approximate the solutions of the peridynamic equations. Other applications of peridynamics for thermo-mechanics or other multi-physics problems can be found in [33–37].

In the context of peridynamic electrical conduction and coupled electro-mechanical models, Prakash and Seidel [6] developed a bond-based formulation for the study of the electrical and piezoresistive response of carbon nanotube reinforced polymer nanocomposite materials. The authors applied then their formulation to model the strain and damage sensing in nanocomposite bonded explosive materials [38,39]. Moreover, electrical conduction in nanocomposite materials, which are of developing interest in the scientific community [40,41], involves also highly non-local processes such as electron hopping [39]. A computational model for electrical conduction based on Peridynamics is advantageous as it not only accounts for nonlocality but it also allows to properly describe the primary field in the vicinity of discontinuities. In fact, unlike other computational paradigms such as the finite element method and the boundary element method in which the nucleation and extension of cracks requires cumbersome procedures such as remeshing [2,42], in Peridynamics solids cracking is a consequence of the movement of material points. This feature makes peridynamics very attractive for the simulation of failure and the interaction between propagating cracks and electrical field variables in electro-mechanical problems. It should be noted that the equations for electrical conduction used by Prakash and Seidel, are based on Bobaru and Duangpanya's formulation for peridynamic heat conduction [29,30], where the primary variable is electrical potential instead of temperature and the flux quantity is electrical current density instead of heat flux [38]. However, since such electro-mechanical model is based on a classical bond-based PD formulation, only one independent elastic material constant can be chosen, whereas the Poisson's ratio result to be fixed.

In this paper, an original micropolar peridynamic (MPPD) formulation recently presented [18], is extended to electro-mechanical problems. Firstly, a novel peridynamic implicit analytical formulation for electrical conduction is derived based on the definition of a specific microelectrical energy function for non-local lattices and a specific electrical inelastic deformation parameter e. The electrical peridynamic model is then coupled with the mechanical micropolar formulation capable to handle variable Poisson's ratios and non-homogeneous deformation fields in isotropic Cauchy solids. A distinctive aspect of the model, that differs from other bond-based PD electromechanical models which are explicit formulations and are affected by the Poisson's ratio restriction, is that each bond connecting two particles can be idealized as an assemblage of three mechanical springs (two translational springs and a rotational spring) and a electrical conductive ligament. The introduction of the mechanical bond shear stiffness and the definition of a bond shearing deformation measure which accounts for particles rotation, enables the model to predict the mechanical behavior of a wide variety of isotropic conductive materials undergoing homogeneous and non-homogeneous deformations, including fracture and piezoresistive response.

It should be noted that the implicit electrical conduction formulation here presented can be also extended to other diffusion problems. Hence, the analytical expression of the electro-mechanical stiffness operator is also useful for thermo-mechanical problems or other multi-physics behaviors. The present model couples for the first time, the intuitive simplicity and physically-based nature of bond-based formulations (removing the Poisson's ratio restriction), with the mathematical formalism, accuracy and numerical stability of analytical implicit formulations [42]. This paper is structured as follows. In Section 2, an analytical implicit linearized formulation of the electro-mechanical micropolar peridynamic model is given. The generalized four-parameter micropolar formulation is derived starting from the definition of three specific deformation measures (i.e. bond's elongation, shear and particles' relative rotation), and an electrical inelastic deformation parameter. Starting from the definition of the microelastic and

Please cite this article as: V. Diana and V. Carvelli, An electromechanical micropolar peridynamic model, Computer Methods in Applied Mechanics and Engineering (2020) 112998, https://doi.org/10.1016/j.cma.2020.112998.

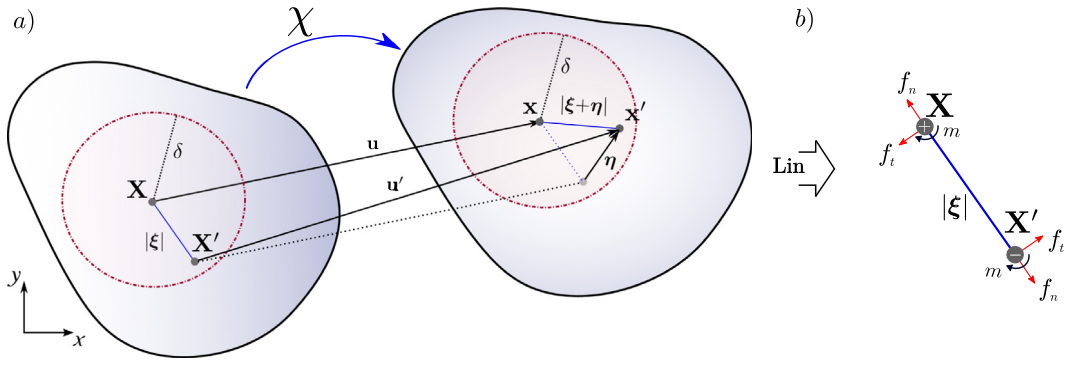

Fig. 1. (a) Undeformed and deformed configurations of a peridynamic body; (b) Linearized framework: The normal and shear components of the pairwise force f are aligned with and normal to the bond connecting the two particles in the undeformed configuration, respectively.

the microelectric energy functions, and imposing the constitutive equation and the compatibility conditions, the expression of the electro-mechanical stiffness operator is derived. The analytical expression of the mechanical and electrical peridynamic constants for isotropic materials are thus obtained. Moreover, a specific damage model for brittle conductive materials is proposed. In Section 3 the accuracy of the proposed implicit PD formulation is illustrated: to solve the Poisson's equation on a circular domain, to predict the electric field potential and electric current density in two square metallic laminae (in the steady-state regime) (Section 3.1), then to assess the electro-mechanical micropolar damage model (Section 3.2), and finally to simulate the piezoresistive behavior of nanocomposite materials (Section 3.3).

2. The unified micropolar electromechanical model

The proposed peridynamic electromechanical model complies with a micropolar formulation [18,43] to overcome the Poisson's ratio restriction in elasticity. It considers augmented translational degrees of freedom including a rotational degree of freedom θ [44]. The linear and angular momentum balance equations for any infinitesimal material particle at position $\mathbf{X}$ and time t in the reference configuration (see Fig. 1) are

$$\int_{H_{\mathbf{X}}} \mathbf{f}(\mathbf{u}' - \mathbf{u}, \mathbf{X}' - \mathbf{X}) dV_{\mathbf{X}'} + \mathbf{b}(\mathbf{X}, t) = \rho \ddot{\mathbf{u}}(\mathbf{X}, t) \quad \text{for} \quad \mathbf{X} \in \Omega, \tag{1}$$

$$\int_{H_{\mathbf{X}}} \mathbf{m}(\mathbf{u}' - \mathbf{u}, \mathbf{X}' - \mathbf{X}) dV_{\mathbf{X}'} + \mathbf{c}(\mathbf{X}, t) = \mathbf{J}\ddot{\boldsymbol{\theta}}(\mathbf{X}, t) \quad \text{for} \quad \mathbf{X} \in \Omega, \tag{2}$$

where Ω is the domain occupied by the body, whereas $\mathbf{X}' - \mathbf{X} = \boldsymbol{\xi}$ and $\mathbf{u}' - \mathbf{u} = \boldsymbol{\eta}$ are the relative position (i.e. reference bond) and the relative displacement between the material points $\mathbf{X}$ and $\mathbf{X}'$ (see Fig. 1). The integrals are defined over a region $H_{\mathbf{X}}$ called the horizon region of radius δ or family of $\mathbf{X}$, as shown in Fig. 1(a). The body force vector is $\mathbf{b}$, and $\mathbf{f}$ is the pairwise force function of the peridynamic bond, having the dimensions of a force per unit volume squared. The applied body couple or body torque vector is indicated by $\mathbf{c}$ and $\ddot{\boldsymbol{\theta}}$ is the angular acceleration vector, while $\mathbf{J}$ denotes the mass moment of inertia per unit volume tensor. The pairwise moment function $\mathbf{m}$ has the dimensions of a couple per unit volume squared.

The balance equation of the peridynamic diffusion problem [6,29], in the specific case of electric conduction is instead

$$\int_{H_{\mathbf{X}}} f_I(\phi' - \phi, \mathbf{u}' - \mathbf{u}, \mathbf{X}' - \mathbf{X}) dV_{\mathbf{X}'} + \boldsymbol{\omega}(\mathbf{X}, t) = \dot{\boldsymbol{\varrho}}(\mathbf{X}, t) \quad \text{for} \quad \mathbf{X} \in \Omega, \tag{3}$$

where ϕ is the particle's electric potential, $\dot{\boldsymbol{\varrho}}$ is the time rate of variation of charge density due to a time variation of the electrical field potential, $\boldsymbol{\omega}$ is the net current per unit volume at $\mathbf{X}$, and f_I is the electric peridynamic kernel (i.e. the integrand function), having the dimensions of an electric current per unit volume squared. The quasi-static equilibrium and steady-state equations are obtained setting the right term of Eqs. (1)–(3) equal to zero (the time

dependent accumulation of electric charge and the dynamic effects in elasticity are neglected). The discretized form of the peridynamic integral balance equations at time t is:

$$\sum_{j=1} \mathbf{f}(\mathbf{u}_j - \mathbf{u}_i, \mathbf{X}_j - \mathbf{X}_i)\Delta V_j + \mathbf{b}_i = \rho \ddot{\mathbf{u}}_\mathbf{i} \tag{4}$$

$$\sum_{j=1} \mathbf{m}(\mathbf{u}_j - \mathbf{u}_i, \mathbf{X}_j - \mathbf{X}_i)\Delta V_j + \mathbf{c}_i = \mathbf{J}\ddot{\boldsymbol{\theta}}_\boldsymbol{i} \tag{5}$$

$$\sum_{j=1} f_I(\phi' - \phi, \mathbf{u}_j - \mathbf{u}_i, \mathbf{X}_j - \mathbf{X}_i)\Delta V_j + \boldsymbol{\omega}_i = \dot{\boldsymbol{\varrho}}_\mathbf{i} \tag{6}$$

where subscript j denotes a particle within the horizon region of particle i. Thus the sum in Eqs. (4)–(6) is over all nodes j such that $|\mathbf{X}_j - \mathbf{X}_i| \leq \delta$ (i.e. neighboring particles of particle i). Each bond connecting two particles i and j can be idealized as an assemblage of three mechanical springs (two translational springs and a rotational spring) and an electrical conductive ligament. Regarding the mechanical model, the particles force and displacement (i.e. the primary field) vectors in the bond local coordinate system are

$$\{f\}^T = \{f_n^i \quad f_t^i \quad m^i \quad f_n^j \quad f_t^j \quad m^j\} \tag{7}$$

and

$$\{u\}^T = \{u_n^i \quad u_t^i \quad \theta^i \quad u_n^j \quad u_t^j \quad \theta^j\} \tag{8}$$

Being the primary field of the electrical model the particles electric potential, the unified electromechanical primary field vector referred to a couple of connected particles can be written as

$$\{u^*\}^T = \{u_n^i \quad u_t^i \quad \theta^i \quad \phi^i \quad u_n^j \quad u_t^j \quad \theta^j \quad \phi^j\} \tag{9}$$

and the vector of the external actions

$$\{f^*\}^T = \{f_n^i \quad f_t^i \quad m^i \quad f_I^i \quad f_n^j \quad f_t^j \quad m^j \quad f_I^j\} \tag{10}$$

This being a linearized micropolar peridynamic formulation, normal and tangential displacements are given with respect to coordinate axes that are aligned with the undeformed configuration (see Fig. 1(b)). Moreover, the bond electric field is oriented along the direction of the ligament in the undeformed configuration. It allows to define three bond deformation parameters (s, γ and ϑ) and an electric one, e (see Fig. 2). The deformation in the normal direction is the bond stretch s,

$$s = \frac{|\boldsymbol{\xi} + \boldsymbol{\eta}| - |\boldsymbol{\xi}|}{|\boldsymbol{\xi}|} \tag{11}$$

which in a linearized theory is

$$s = \frac{1}{|\boldsymbol{\xi}|}\left(\boldsymbol{\eta} \cdot \frac{\boldsymbol{\xi}}{|\boldsymbol{\xi}|}\right) = \frac{\eta_n}{|\boldsymbol{\xi}|} = \frac{(u_n^j - u_n^i)}{|\boldsymbol{\xi}|} \tag{12}$$

where η_n is the component of $\boldsymbol{\eta}$ along the undeformed bond of unit vector $\boldsymbol{\xi}/|\boldsymbol{\xi}|$. The shearing deformation or bond sliding is

$$\gamma = \frac{(u_t^j - u_t^i)}{|\boldsymbol{\xi}|} - \frac{(\theta^j + \theta^i)}{2} \tag{13}$$

defined as the difference between the rotation angle of the bond and the particles average rotation. The latter reduces or increases the bond sliding depending on the mutual rotation of the particles. In particular, if the two particles rotate with an equal and opposite angle θ, the rotation contribution to the bond sliding is null. The deformation parameter corresponding to the rotational bond spring is instead the relative particles' rotation measure, or, in other words, the difference between the rotation angles of the two connected particles

$$\vartheta = (\theta^j - \theta^i) \tag{14}$$

Please cite this article as: V. Diana and V. Carvelli, An electromechanical micropolar peridynamic model, Computer Methods in Applied Mechanics and Engineering (2020) 112998, https://doi.org/10.1016/j.cma.2020.112998.

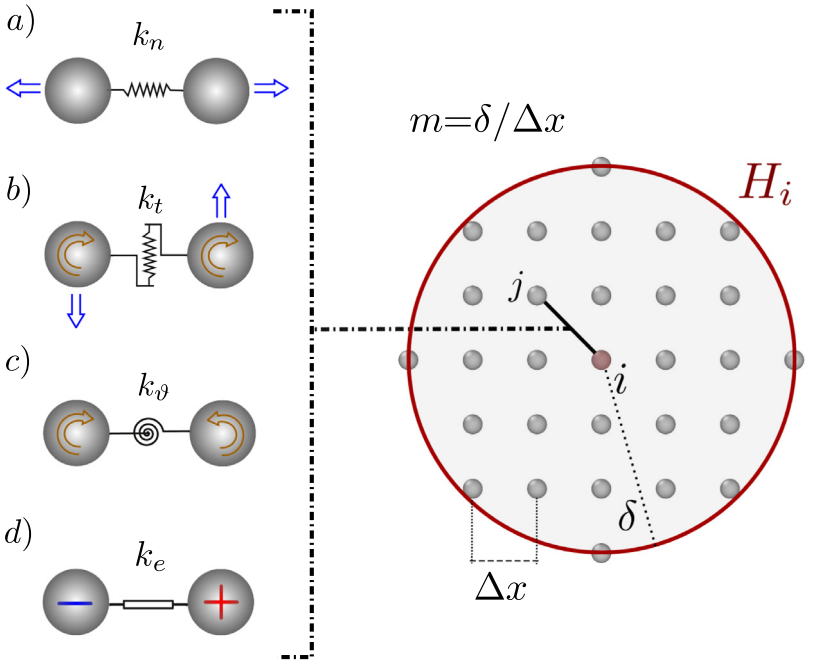

Fig. 2. Sketch of the interactions between two particles: (a) mechanical normal spring, (b) mechanical shearing spring, (c) mechanical rotational spring, (d) conductive bond.

In the peridynamic electrical model, the parameter e, function of the bond electric field,[1] and defined as

$$e = -\frac{(\phi^j - \phi^i)}{|\boldsymbol{\xi}|} \tag{16}$$

is considered as the equivalent of a deformation measure in elasticity. Hence, we can write the compatibility equation relating the particles displacements to the bond deformation parameters

$$\{h\} = [B]^T \{u\} \tag{17}$$

where $\{h\} = \{s \quad \gamma \quad \vartheta\}^T$ is the vector of the springs' deformation measures and $[B]^T$ is defined as

$$[B]^T = \frac{1}{|\boldsymbol{\xi}|} \begin{bmatrix} -1 & 0 & 0 & 1 & 0 & 0 \\ 0 & -1 & -|\boldsymbol{\xi}|/2 & 0 & 1 & -|\boldsymbol{\xi}|/2 \\ 0 & 0 & -|\boldsymbol{\xi}| & 0 & 0 & |\boldsymbol{\xi}| \end{bmatrix} \tag{18}$$

Moreover the relationship between the bond electric field parameter e and the particles electric potentials is

$$e = \{b\}^T \{\phi\} \tag{19}$$

where $\{\phi\} = \{\phi_i \quad \phi_j\}^T$ and

$$\{b\}^T = -\frac{1}{|\boldsymbol{\xi}|}\{-1 \quad 1\} \tag{20}$$

[1] The bond electric field is defined by

$$\boldsymbol{e} = -\frac{(\phi^j - \phi^i)}{|\boldsymbol{\xi}|}\frac{\boldsymbol{\xi}}{|\boldsymbol{\xi}|} \tag{15}$$

The constitutive behavior of the mechanical model is defined by the following relation

$$\{q\} = [D]\{h\} \longrightarrow \begin{Bmatrix} f_n \\ f_t \\ m_\vartheta \end{Bmatrix} = \begin{bmatrix} k_n & 0 & 0 \\ 0 & k_t & 0 \\ 0 & 0 & k_\vartheta \end{bmatrix} \begin{Bmatrix} s \\ \gamma \\ \vartheta \end{Bmatrix} \tag{21}$$

where $[D]$ is a diagonal matrix[2] containing the bond normal, tangential, and rotational spring equivalent stiffnesses, and relates the pairwise forces and micromoment to the parameters of the bond deformation defined previously. The pairwise bond moment and forces can be considered as the springs reactions to the bond deformations s and γ and ϑ, respectively. In particular, considering a single bond, the bond forces are equal in modulus to the particles forces divided by the product of the particles volumes. It must be highlighted that, m_i and m_j could assume the same nonzero value leading to a bond micromoment m_ϑ equal to zero [18]. In fact, m_ϑ represents the self-equilibrated part of the particles micromoments in a specific ligament.

It should be noted that this is a general micropolar peridynamic formulation that can lead to different centrosymmetric models depending on the specific constitutive parameters k_n, k_t and k_ϑ adopted for each bond [18]. Moreover, the shear stiffness parameter k_t has the same dimensions (force per unit volume squared) of the normal stiffness parameter k_n and is conceptually related to the shear modulus G of classical elasticity [18]. In fact, the stiffness k_t is directly related to the shear bond forces through the shear deformation parameter previously defined, similar to the relationship among G, τ and the shear deformation γ^* in classical elasticity [19]. It is interesting to note that the micropolar peridynamic model with frame-like ligaments connecting particles (a 2D non-local lattice with Euler–Bernoulli beam-like microstructure, e.g. Gerstle's isotropic micropolar model [44]), is a special case of the conceived model described in this section. Further details can be found in [19,43]. The constitutive equation of the electrical model is

$$q_I = k_e\, e \tag{22}$$

It relates the magnitude of the bond micro current density (or peridynamic bond current–flux) to the bond electric field parameter e.[3] The bond micro current density magnitude is

$$q_I = -\frac{k_e(\phi' - \phi)}{|\boldsymbol{\xi}|} \tag{23}$$

In Eq. (23), k_e is the microconductivity of the peridynamic electrical model,[4] having the dimension of an electric conductivity per unit volume.

The general form of the mechanical macroelastic energy density $\Phi(\mathbf{X})$ for micropolar peridynamics is obtained assuming the contribution of the three springs and their corresponding deformation measures. Three microelastic potential functions can be defined such that

$$\Phi(\mathbf{X}) = \frac{1}{2}\int_{H_\mathbf{X}} \mathrm{w}\, dV_{\mathbf{X}'} = \frac{1}{2}\int_{H_\mathbf{X}} (\mathrm{w_s} + w_\gamma + w_\vartheta) dV_{\mathbf{X}'} = \frac{1}{2}\int_{H_\mathbf{X}} \left(\frac{k_n s^2|\boldsymbol{\xi}|}{2} + \frac{k_t \gamma^2 |\boldsymbol{\xi}|}{2} + \frac{k_\vartheta \vartheta^2}{2}\right) dV_{\mathbf{X}'} \tag{24}$$

Then the definition of the macroelastic potential energy for a micropolar peridynamic body is

$$\hat{\Phi} = \frac{1}{2}\int_\Omega \int_{H_\mathbf{X}} \left(\frac{k_n s^2|\boldsymbol{\xi}|}{2} + \frac{k_t \gamma^2 |\boldsymbol{\xi}|}{2} + \frac{k_\vartheta \vartheta^2}{2}\right) dV_{\mathbf{X}'} dV_\mathbf{X} \tag{25}$$

For a single bond of length $|\boldsymbol{\xi}|$ between two particles i and j (Fig. 3), the discrete form of the balance of the variation of the total macroelastic energy and the work W of the external nodal forces $\{p\}$ is

$$\hat{\Phi} = \frac{1}{2}\{u\}^T \frac{1}{2}[B][D]\Delta V_i [\xi]\alpha \Delta V_j [B]^T \{u\} = \frac{1}{2}\{u\}^T \{p\} = W \tag{26}$$

[2] When considering orthotropic materials, the $[D]$ matrix which describes the constitutive behavior of the bond is dependent on the orientation (ψ) angle of the ligament.

[3] In vectorial form is $\boldsymbol{q_I} = k_e\, \boldsymbol{e}$.

[4] A piezoresistive behavior could be modeled considering the microconductivity k_e function of a deformation measure such as the elastic stretch s, i.e. $k_e = k_e(s)$.

Please cite this article as: V. Diana and V. Carvelli, An electromechanical micropolar peridynamic model, Computer Methods in Applied Mechanics and Engineering (2020) 112998, https://doi.org/10.1016/j.cma.2020.112998.

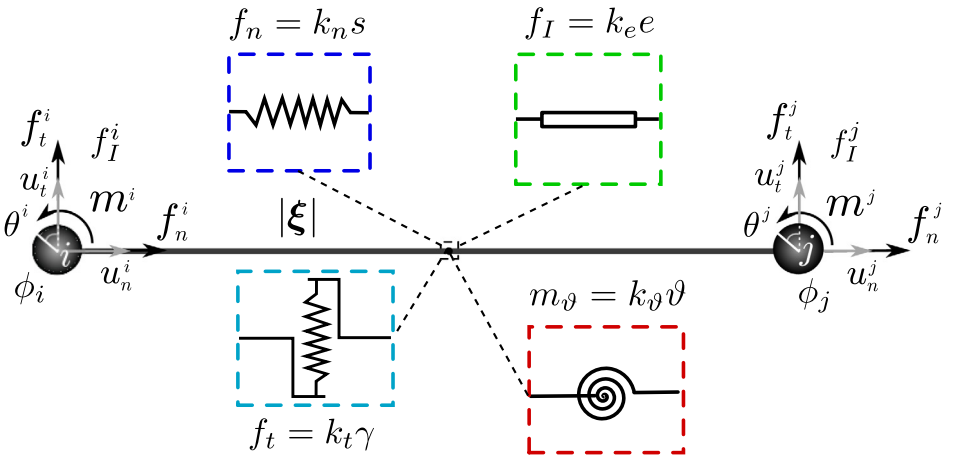

Fig. 3. Schematics of bond configuration connecting two particles i and j in the local coordinate system for electromechanical micropolar peridynamics. The bond can be idealized as a set of three mechanical (axial, shear and rotational), and one electrical conductive equivalent elements.

where, due to Eq. (24)

$$[\xi] = \begin{bmatrix} |\boldsymbol{\xi}| & 0 & 0 \\ 0 & |\boldsymbol{\xi}| & 0 \\ 0 & 0 & 1 \end{bmatrix} \tag{27}$$

Hence, the elasticity bond stiffness matrix in the global coordinate system can be expressed as

$$[K]_{elasticity} = \alpha \Delta V_i \Delta V_j [R]^T [B][D][\xi][B]^T [R] \tag{28}$$

where $[R]$ is a rotation matrix whose terms depend on the specific orientation of the bond in the space and α is the volume correction coefficient that takes into account the partial neighbor intersection [45]

$$\alpha(|\boldsymbol{\xi}|) = \begin{cases} \frac{|\boldsymbol{\xi}| - \delta + 0.5\Delta x}{\Delta x} & \text{if} \quad (\delta - 0.5\Delta x) < |\boldsymbol{\xi}| \leq \delta \\ 1 & \text{if} \quad |\boldsymbol{\xi}| \leq (\delta - 0.5\Delta x) \\ 0 & \text{otherwise} \end{cases} \tag{29}$$

where Δx is the grid spacing.

Similarly, the analytical expression of the electrical stiffness operator is obtained by defining the peridynamic macroelectrical energy density as

$$\Phi_e(\mathbf{X}) = \frac{1}{2} \int_t \int_{H_\mathbf{X}} \mathrm{w}_e \, \mathrm{dV}_{\mathbf{X}'} \, \mathrm{d}t = \frac{1}{2} \int_t \int_{H_\mathbf{X}} \frac{k_e e^2}{2} \, \mathrm{dV}_{\mathbf{X}'} \, \mathrm{d}t = \frac{1}{2} \int_t \int_{H_\mathbf{X}} \frac{k_e (\phi' - \phi)^2}{2|\boldsymbol{\xi}|^2} \, \mathrm{dV}_{\mathbf{X}'} \, \mathrm{d}t \tag{30}$$

thus the expression of the macroelectric power density

$$P_e(\mathbf{X}) = \frac{1}{2} \int_{H_\mathbf{X}} \mathrm{w}_e \, \mathrm{dV}_{\mathbf{X}'} = \frac{1}{2} \int_{H_\mathbf{X}} \frac{k_e e^2}{2} \, \mathrm{dV}_{\mathbf{X}'} \tag{31}$$

By following the procedure described above for the mechanical model, the discrete form of the balance of the variation of the macroelectrical energy (or the electrical power) and the external electrical work W_e leads to

$$[K]_{electrical} = \alpha \Delta V_i \Delta V_j [R^*]^T \{b\} k_e \{b\}^T [R^*] \tag{32}$$

where in this case $[R^*]$ is an identity matrix. The unified electromechanical bond stiffness operator in the global coordinate system, in the hypothesis of small displacements/deformations, can be expressed as

$$[K]_{bond} = \alpha \Delta V_i \Delta V_j [R^u]^T [K][R^u] \tag{33}$$

Please cite this article as: V. Diana and V. Carvelli, An electromechanical micropolar peridynamic model, Computer Methods in Applied Mechanics and Engineering (2020) 112998, https://doi.org/10.1016/j.cma.2020.112998.

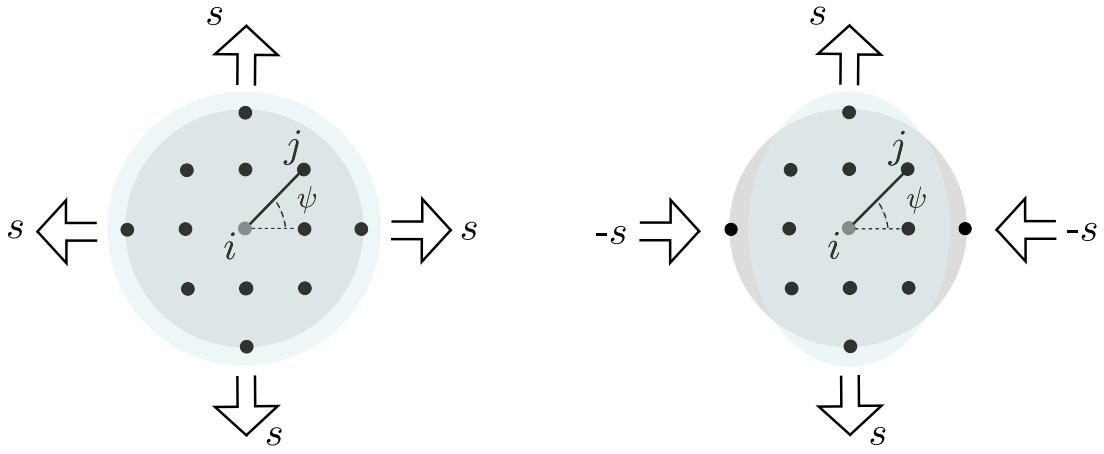

Fig. 4. Schematics of H_x subjected to: (a) isotropic expansion field of orthogonal PD stretch components $s_1 = s_2 = s$; (b) pure shear field of orthogonal PD stretch components $s_1 = -s_2 = s$.

where $[R^u]$ is the rotation matrix of the unified electro-mechanical model and

$$[K] = \frac{1}{|\boldsymbol{\xi}|}\begin{bmatrix} k_n & 0 & 0 & 0 & -k_n & 0 & 0 & 0 \\ 0 & k_t & k_t|\boldsymbol{\xi}|/2 & 0 & 0 & -k_t & k_t|\boldsymbol{\xi}|/2 & 0 \\ 0 & k_t|\boldsymbol{\xi}|/2 & k_\theta|\boldsymbol{\xi}| + k_t|\boldsymbol{\xi}|^2/4 & 0 & 0 & -k_t|\boldsymbol{\xi}|/2 & -k_\theta|\boldsymbol{\xi}| + k_t|\boldsymbol{\xi}|^2/4 & 0 \\ 0 & 0 & 0 & k_e/|\boldsymbol{\xi}| & 0 & 0 & 0 & -k_e/|\boldsymbol{\xi}| \\ -k_n & 0 & 0 & 0 & k_n & 0 & 0 & 0 \\ 0 & -k_t & -k_t|\boldsymbol{\xi}|/2 & 0 & 0 & k_t & -k_t|\boldsymbol{\xi}|/2 & 0 \\ 0 & k_t|\boldsymbol{\xi}|/2 & -k_\theta|\boldsymbol{\xi}| + k_t|\boldsymbol{\xi}|^2/4 & 0 & 0 & -k_t|\boldsymbol{\xi}|/2 & k_\theta|\boldsymbol{\xi}| + k_t|\boldsymbol{\xi}|^2/4 & 0 \\ 0 & 0 & 0 & -k_e/|\boldsymbol{\xi}| & 0 & 0 & 0 & k_e/|\boldsymbol{\xi}| \end{bmatrix} \tag{34}$$

It can be noted that in Eqs. (24) and (30), the factor 1/2 is included because the energy stored in each bond is associated equally with the two particles connected by the ligament. Therefore, Eqs. (28) and (32) provide the expression of the half-bond stiffness matrix. For this reason, being Eq. (34) referred to the entire bond, the factor 1/2 is removed. Moreover, assuming geometrical effects on the electrical solution, the actual (deformed) bond length $|\boldsymbol{\xi} + \boldsymbol{\eta}|$ has to be considered. Hence, $k_e/|\boldsymbol{\xi}|^2$ is replaced by $k_e/|\boldsymbol{\xi} + \boldsymbol{\eta}|^2$ in Eq. (34). After the assembly of the global stiffness matrix, the displacements and the electric potentials can be determined.

In the present implementation, the volume method for correcting the peridynamic surface effect is adopted [42, 46].

2.1. Electromechanical constants

The relationship between the microelastic and microelectrical constants of the unified electromechanical model and the conventional continuum parameters can be obtained by equating the microelastic energy function of micropolar peridynamic model to the conventional strain energy density in elasticity (for two different homogeneous deformation fields) and by equating the peridynamic microelectrical energy (power) density to the classical electrical energy (power) density for an assigned homogeneous electrical field. As for the mechanical constants, we consider an isotropic expansion ($s_1 = s_2 = \varepsilon$) and a pure shear deformation with $s_1 = -s_2 = s$ (see Fig. 4). The analytical expressions of the two classical continuum strain energy densities and the corresponding micropolar peridynamic macroelastic energy density functions are derived in Appendix.

Thus, solving the systems of Eqs. (A.3)–(A.5) and Eqs. (A.7)–(A.9) for k_n and k_t, the following relations are obtained:

$$k_n = \frac{6E}{\pi t \delta^3 (1-\nu)}; \qquad k_t = \frac{6E(1-3\nu)}{\pi t \delta^3 (1-\nu^2)} \tag{35}$$

Please cite this article as: V. Diana and V. Carvelli, An electromechanical micropolar peridynamic model, Computer Methods in Applied Mechanics and Engineering (2020) 112998, https://doi.org/10.1016/j.cma.2020.112998.

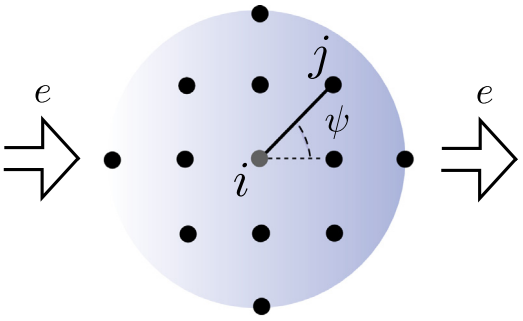

Fig. 5. Schematics of H_x subjected to a horizontal linear variation of electric potential ϕ.

$$k_n = \frac{6E}{\pi \mathrm{t}\delta^3(1-2\nu)(1+\nu)}; \qquad k_t = \frac{6E(1-4\nu)}{\pi \mathrm{t}\delta^3(1-2\nu)(1+\nu)} \tag{36}$$

for plane stress and plane strain, respectively.

The microelectric energy function in isotropic peridynamics is described by Eq. (30) and in the specific case of a linear potential variation in the horizontal direction (i.e. in the case of homogeneous electric field $\boldsymbol{e} = \boldsymbol{e_x}$ as described in Fig. 5), we can write

$$\begin{aligned}\Phi_e(\mathbf{X}) &= \frac{1}{2}\int_t\int_{H_\mathbf{X}} \frac{k_e(\phi'-\phi)^2}{2|\boldsymbol{\xi}|^2}\,\mathrm{dV}_{\mathbf{X}'}\,\mathrm{d}t = \frac{1}{2}\int_t\int_{H_\mathbf{X}} \frac{k_e e^2}{2}\,\mathrm{d}V_{\mathbf{X}'}\,\mathrm{d}t \\ &= \frac{1}{2}\int_t\int_{H_\mathbf{X}} \frac{k_e \mathrm{t} e^2\cos^2(\psi)}{4}\,\mathrm{d}A_{\mathbf{X}'}\,\mathrm{d}t = \frac{1}{2}\int_t\int_0^\delta 4\int_0^{\pi/2} \frac{k_e \mathrm{t} e^2\cos^2(\psi)|\boldsymbol{\xi}|}{2}\,\mathrm{d}\psi\, d\xi\,\mathrm{d}t \\ &= \int_t \frac{k_e \mathrm{t}\pi e^2\delta^2}{8}\mathrm{d}t\end{aligned} \tag{37}$$

considering that t is the thickness, and that in this specific case the bond electric field parameter e depends on the bond orientation angle ψ by

$$e(\psi) = e\cos(\psi) \tag{38}$$

The corresponding quantity in classical continuum is

$$\int_t \frac{K_e e^2}{2}\mathrm{d}t \tag{39}$$

where K_e is the electrical conductivity of the material. Hence we obtain

$$k_e = \frac{4K_e}{\pi \mathrm{t}\delta^2} \tag{40}$$

that is the same expression of k_e obtained in [29] following a different approach.

Remark 1. The proposed mechanical micropolar model is a physically-based model inspired by Voigt's studies on crystals [17,47]. The particles' rotational degree of freedom that characterizes the mechanical model fulfill the fundamental requirement of rotational invariance. In fact, the microrotations and the micromoments ensure the balance of angular momentum of the ligament. The definition of a shearing deformation measure that does not account for particle rotations, could lead to an incorrect description of the mechanical behavior of materials undergoing non-homogeneous deformation fields [19].[5] However, when referring to an isotropic Cauchy continuum, the definition of an equivalent lattice model requires only two elastic moduli, and thus the definition of a rotational spring constant k_ϑ is redundant. A theoretical discussion on this aspect, that is related to the so called "Cauchy relations", can be found in [52] while some examples of lattices were shown in [18,53,54].

[5] When using a non micropolar model that accounts for bond shear deformability, special treatments could be needed for calculating the shear displacement and avoiding local rigid body rotations [48–51].

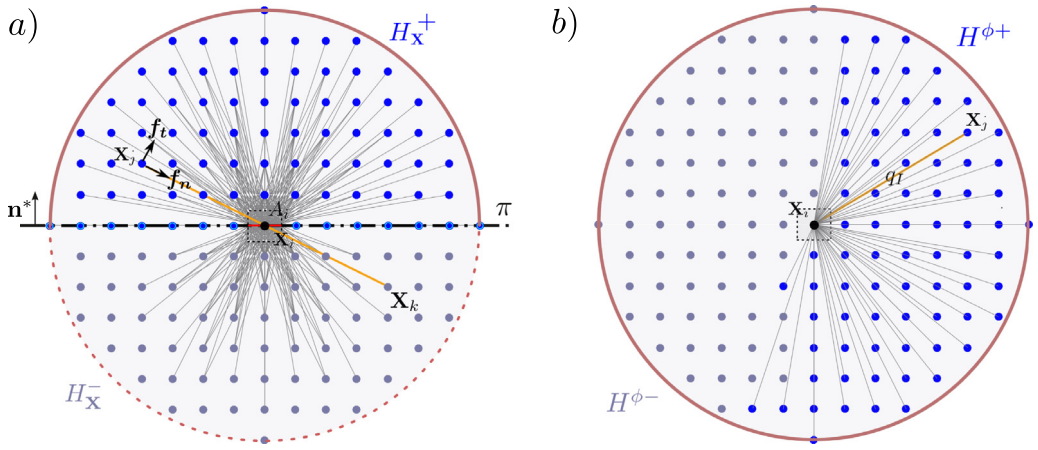

Fig. 6. (a) Definition of the micropolar PD traction vector at point $\mathbf{X_i}$ according to Eq. (44) with respect to plane π of outward unit normal $\mathbf{n}^*$. The pairwise force $\mathbf{f}$ is characterized by normal and tangential components $\mathbf{f_n}$ and $\mathbf{f_t}$; (b) Definition of the peridynamic electrical current density magnitude in the case of a non-homogeneous electric field. (For interpretation of the references to color in this figure legend, the reader is referred to the web version of this article.)

Remark 2. The presence of rotational moduli introduces internal lengths into the parameters governing the elasticity response. It is otherwise strictly needed when modeling a micro-polar material, e.g. a Cosserat continuum, or when modeling at the macroscale a composite material having an internal periodic structure, which is explicitly affected by the size and shape of the microstructure [54]. In the present model, it can improve the numerical performance of the discrete approximation in the case of non-homogeneous strain conditions, and it allows to describe variable axial bond forces with a reduced number of elements [54,55]. Therefore, it can be stated that the introduction of the rotational stiffness term allows an improvement of the numerical model in the case of high strain gradient, especially for a very coarse mesh [19].

2.2. The mechanical stress and the electric charge flux

The stress definition used in this work is based on Lehouq and Silling's force flux formulation [56] which is extended here to micropolar peridynamics. The aforementioned stress concept is strictly related to the original stress definition by Saint Venant [57] and accepted later by Cauchy [56,58] in the early days of elasticity. For more details on the concept of stress in peridynamics, see [43,56,59,60].

Considering an arbitrary plane π passing through $\mathbf{X}$ which has a normal vector $\mathbf{n}^*$ and divides the family region $H_{\mathbf{X}}$ into two pieces (Fig. 6), the force which one part exerts on the other can be expressed as

$$\mathbf{F}(H_{\mathbf{X}^+}, H_{\mathbf{X}^-}) = \int_{H_{\mathbf{X}}^-} \int_{H_{\mathbf{X}}^+} \mathbf{f}(\mathbf{u}'' - \mathbf{u}', \mathbf{X}'' - \mathbf{X}') dV_{\mathbf{X}''} V_{\mathbf{X}'} \tag{41}$$

The segment $\mathbf{X}'' - \mathbf{X}'$, given by the couple of interacting points, intersects the plane π at a unique point $\mathbf{X}$. The segment $\mathbf{X}'' - \mathbf{X}$ has the length ζ and points in the outer direction $\mathbf{v}$, i.e. $\mathbf{v} \cdot \mathbf{n}^* > 0$. The segment $\mathbf{X} - \mathbf{X}'$ has the length υ and points in the opposite direction such that

$$\mathbf{X}'' = \mathbf{X} + \zeta \mathbf{v}; \qquad \mathbf{X}' = \mathbf{X} - \upsilon \mathbf{v} \tag{42}$$

The integration over all interacting couples $[\mathbf{X}''; \mathbf{X}']$ Eq. (41) can be rewritten as a surface integral over the contact plane π of a corresponding surface density, i.e. the traction vector $\mathbf{t}(\mathbf{X}, \mathbf{n}^*)$ [60]. Hence, the PD traction vector with respect to plane π, with outward unit normal $\mathbf{n}^*$ at point $\mathbf{X}$ is now defined by [56]

$$\mathbf{t}(\mathbf{X}, \mathbf{n}^*) = \frac{1}{2} \int_{\mathcal{L}} \int_0^{\delta} \int_0^{\delta} (\zeta + \upsilon)^2 \mathbf{f}[\mathbf{u}'' - \mathbf{u}', \mathbf{v}(\zeta + \upsilon)] \mathbf{v} \cdot \mathbf{n}^* d\zeta d\upsilon d\omega_{\mathbf{v}} \tag{43}$$

where $\mathcal{L}$ denotes the unit sphere, and $d\omega_{\mathbf{v}}$ denotes a differential solid angle on $\mathcal{L}$ in the direction of any unit vector $\mathbf{v}$. The factor of $1/2$ in Eq. (43) considers the forces on $\mathbf{X}'$ due to $\mathbf{X}''$ and those on $\mathbf{X}''$ due to $\mathbf{X}'$ [5,56]. Eq. (43) can be simplified and written in discrete form as

$$\mathbf{t}(\mathbf{X}_i, \mathbf{n}^*) = \frac{1}{A_i} \sum_{k=1}^{H^-} \sum_{j=1}^{H+} \mathbf{f}(\mathbf{u}_j - \mathbf{u}_k, \mathbf{X}_j - \mathbf{X}_k) \Delta V_j \Delta V_k$$
$$= \frac{1}{A_i} \sum_{k=1}^{H^-} \sum_{j=1}^{H+} \left[f_n(\mathbf{u}_j - \mathbf{u}_k, \mathbf{X}_j - \mathbf{X}_k) \frac{\boldsymbol{\eta}_n}{|\boldsymbol{\eta}_n|} + f_t(\mathbf{u}_j - \mathbf{u}_k, \mathbf{X}_j - \mathbf{X}_k) \frac{\boldsymbol{\eta}_t}{|\boldsymbol{\eta}_t|} \right] \Delta V_j \Delta V_k \tag{44}$$

where H^- is the number of particles in the negative side of the i-particle's horizon, and $A_i = 2\delta t$ denotes the cross-sectional area of the volume ΔV_i associated with the i-particle (reported in red in Fig. 6). The summation involves only the set of bonds passing through or ending at the cross section A_i from the positive side (gray bonds in Fig. 6). Being this a micropolar model, the pairwise force $\mathbf{f}$ is characterized by normal and tangential components $\boldsymbol{f_n}$ and $\boldsymbol{f_t}$. The normal and tangential components of the traction vector defined above are the normal and the shear stress

$$\sigma_{n^*n^*} = \mathbf{t}(\mathbf{X}_i, \mathbf{n}^*) \cdot \mathbf{n}^* \tag{45}$$
$$\tau_{n^*v} = \mathbf{t}(\mathbf{X}_i, \mathbf{n}^*) \cdot \mathbf{v} \tag{46}$$

where $\mathbf{v}$ denotes the direction orthogonal to the outer normal $\mathbf{n}^*$.

The formulation of the magnitude of the electric current density or electric charge flux $q = |\boldsymbol{q}|$ at $\mathbf{X}$ can be obtained instead from the definition of the bond micro current density magnitude q_I given in Eq. (23). In fact, computing the integral of micro fluxes through all the conductive bonds that connect $\mathbf{X}$ with other material points $\mathbf{X}'$ within the horizon and have a higher electric potential ϕ' than $\mathbf{X}$, we obtain

$$\boldsymbol{q}(\mathbf{X}) = \int_{\mathcal{H}_{\mathbf{X}}^*} \boldsymbol{q_I}\, dV_{\mathbf{X}'} = \int_{\mathcal{H}_{\mathbf{X}}^*} -\frac{k_e(\phi' - \phi)}{|\boldsymbol{\xi}|} \frac{\boldsymbol{\xi}}{|\boldsymbol{\xi}|}\, dV_{\mathbf{X}'} \tag{47}$$

where $\mathcal{H}_{\mathbf{X}}^*$ is the neighboring region of $\mathbf{X}$ satisfying the condition $\phi' > \phi$. Assuming $H^{\phi+}$ as the number of particles such that $\phi_j > \phi_i$, Eq. (47) can be written in discrete form (see Fig. 6) as

$$\boldsymbol{q}(\mathbf{X}_i) = \sum_{j=1}^{H^{\phi+}} -\frac{k_e(\phi_j - \phi_i)}{|\boldsymbol{\xi}_{ij}|} \frac{\boldsymbol{\xi}_{ij}}{|\boldsymbol{\xi}_{ij}|} \Delta V_j \tag{48}$$

that is formally the same equation proposed by Bobaru for the peridynamic heat flux [29]. The bonds that contribute to the current–flux are only those ending at the material point under consideration (gray bonds in Fig. 6). However it is also possible to define the current–flux through the surface at a point by including all bonds passing through that surface, as in the peridynamic formulation for the "force fluxes" [29,56]. The equivalence of the two different ways for introducing the peridynamic flux has been demonstrated by Chen and Bobaru [61] in the case of heat-transfer problems.

2.3. The electromechanical damage model

Several failure criteria for the micropolar peridynamic model have been proposed [18], and since this work focuses on isotropic conductive brittle materials, an extension of the critical stretch failure criterion [62,63] to micropolar peridynamics is considered in this work. For homogeneous isotropic brittle materials, cracks propagate along a mode I path, hence the critical stretch criterion leads to well simulated failure conditions and realistic crack paths even for pure mode II remote loads [64–66]. In particular we consider the classical microelastic brittle damage model [62], in which the ultimate tensile stretch limit or critical stretch s_{ut} is related to the fracture energy for mode I, G_{Ic}

$$G_{Ic} = 2 \int_0^{\delta} \int_z^{\delta} \int_0^{\cos^{-1}(z/|\boldsymbol{\xi}|)} w_s |\boldsymbol{\xi}| t |\boldsymbol{\xi}|\, \mathrm{d}\phi\, \mathrm{d}\xi\, \mathrm{d}z \tag{49}$$

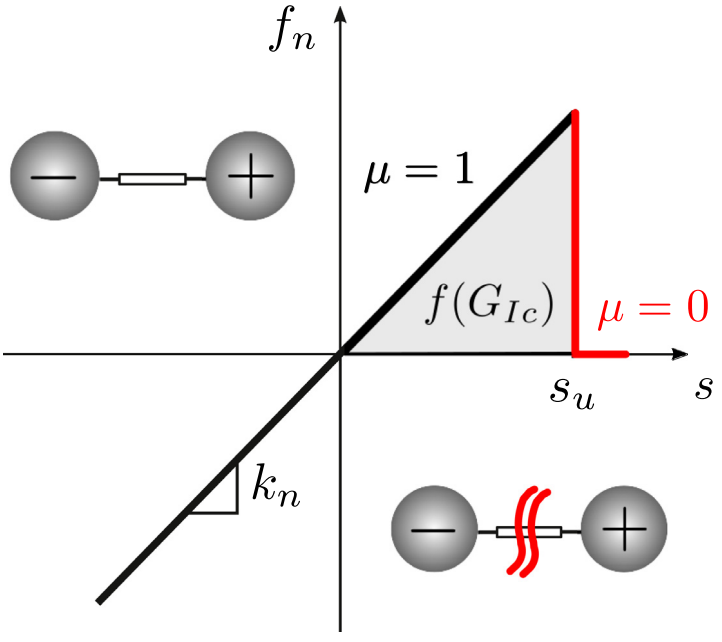

Fig. 7. Axial force–axial deformation constitutive relationship in peridynamic microelastic brittle material with electrically conductive bonds. If the stretch s in specific bond connecting two particles i and j reaches the ultimate value s_u, that bond becomes not electrically conductive.

where, $w_s|\boldsymbol{\xi}|$ is the micro work required to separate a single bond, and $w_s = \mathrm{w_s}/|\boldsymbol{\xi}|$, i.e. the micropotential energy function of the axial spring when $s = s_u$. Considering that in our model the micropotential function $\mathrm{w_s}$ is dependent on the Poisson's ratio of the material, Eq. (49) solved for s_u results in

$$s_u = \sqrt{\frac{4G_{Ic}}{k_n \delta^4 \mathrm{t}}} \tag{50}$$

Adopting a critical stretch criterion, we refer to the mechanical behavior of the equivalent axial spring, being the deformation control carried out exclusively on the bond stretch measure. In order to specify the status of a specific bond $\boldsymbol{\xi}_{ij}$ connecting two particles $\mathbf{X}_i$ and $\mathbf{X}_j$, a history-dependent scalar valued function μ is introduced [62]

$$\mu(\boldsymbol{\xi}_{ij}, t) = \begin{cases} 0 & s \geq s_u \\ 1 & s < s_u \end{cases} \tag{51}$$

Then, based on the function $\mu(\boldsymbol{\xi}_{ij}, t)$, a local tensile damage variable is defined and computed at each time step t and for each particle $\mathbf{X}_i$ as

$$d(\mathbf{X}_i, t) = 1 - \frac{\sum_{j=1} \mu(\boldsymbol{\xi}_{ij}, t) \Delta V_j}{\sum_{j=1} \Delta V_j} \tag{52}$$

The numerator in Eq. (52) represents the actual damaged volume of the unit cell, whereas the denominator is the volume of the family of particle $\mathbf{X}_i$ in the undeformed configuration. Moreover, if the stretch s in specific bond connecting two particles i and j reaches the ultimate value s_u, that bond becomes not electrically conductive (Fig. 7), and this aspect makes the model particularly suitable for damage sensing applications. In other words we assume that

$$k_e = k_e(\mu, K_e, \mathrm{t}, \delta) \tag{53}$$

According to the fracture model here discussed, the electrical conduction is influenced by the propagation of cracks in the structure, however we explicitly assume that the electrical field within the solid does not influence the fracture process.

Please cite this article as: V. Diana and V. Carvelli, An electromechanical micropolar peridynamic model, Computer Methods in Applied Mechanics and Engineering (2020) 112998, https://doi.org/10.1016/j.cma.2020.112998.

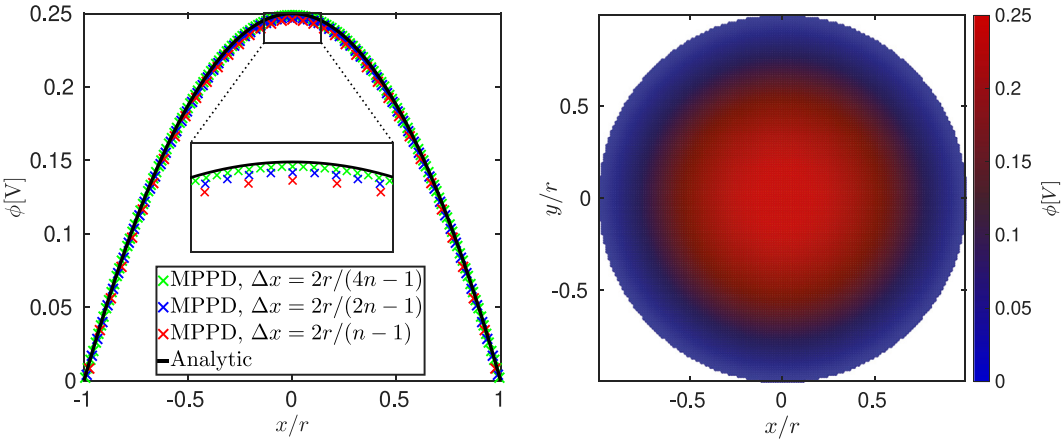

Fig. 8. Poisson's equation on a circular domain of unit radius r. Electric field potential ϕ: (left) δ-convergence study along $y/r = 0$; (right) peridynamic numerical solution obtained adopting $m = 3$ and $\Delta x = 2r/(4n-1)$.

Table 1
Poisson's equation on a circular domain of unit radius r: Discretization adopted and average error of the electric field potential ϕ along $y/r = 0$ with respect to analytical solution.

Δx	n. Particles	ϕ: err. (%)
$2r/(n-1)$	1201	4.52
$2r/(2n-1)$	4905	2.60
$2r/(4n-1)$	19 869	1.45

3. Validation of the model

The accuracy of the proposed implicit PD formulation is first assessed with the Poisson's equation on a circular domain. Hence, it is adopted to predict the electric field potential and electric current density in two square metallic laminae (in the steady-state regime) (Section 3.1), then to assess the electro-mechanical micropolar damage model (Section 3.2). Finally the coupled electromechanical model is applied to simulate the piezoresistive behavior of nanocomposite materials (Section 3.3).

3.1. Electrical conductivity

The Poisson's equation given by

$$-\nabla^2\phi(x, y) = \omega(x, y) \tag{54}$$

and defined on a two-dimensional circular domain Ω of unit radius r is considered as preliminary validation test. However, considering the universal nature of partial differential equations, the results demonstrate the capabilities of the proposed formulation for describing generic physical phenomena governed by elliptic partial differential equations.

A constant source function $\omega(x, y) = 1$ on the domain Ω, and zero boundary conditions on the boundary $\partial\Omega$ are assumed. The conductivity of the material K_e is set to unit for simplicity. The analytical solution

$$\phi(x, y) = \frac{1 - x^2 - y^2}{4} \tag{55}$$

is compared with the peridynamic numerical solutions corresponding to $m = 3$, and adopting three different and decreasing sizes of the grid spacing ($\Delta x = 2r/(n-1)$, $\Delta x = 2r/(2n-1)$ and $\Delta x = 2r/(4n-1)$ with $n = 40$, respectively). It should be noted that since Peridynamics is a non-local model, boundary conditions are applied to a circular boundary layer of finite thickness Λ (in our case $\Lambda = \delta/2$). The results obtained from the simulations, which are shown in Fig. 8 and Table 1, are in good agreement with the analytical solution.

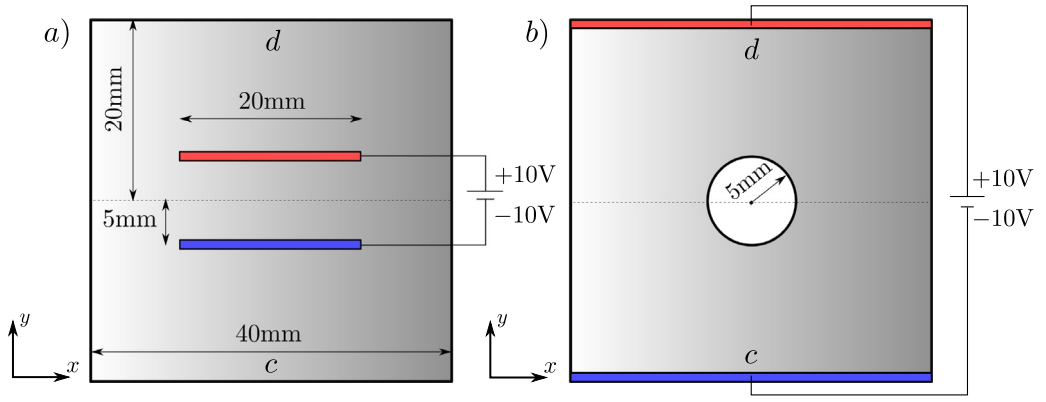

Fig. 9. Square metallic laminae subjected to two different electrical boundary conditions. The zones in which the value of the electric potential is assigned are colored in red (positive value) and in blue (negative value). (For interpretation of the references to color in this figure legend, the reader is referred to the web version of this article.)

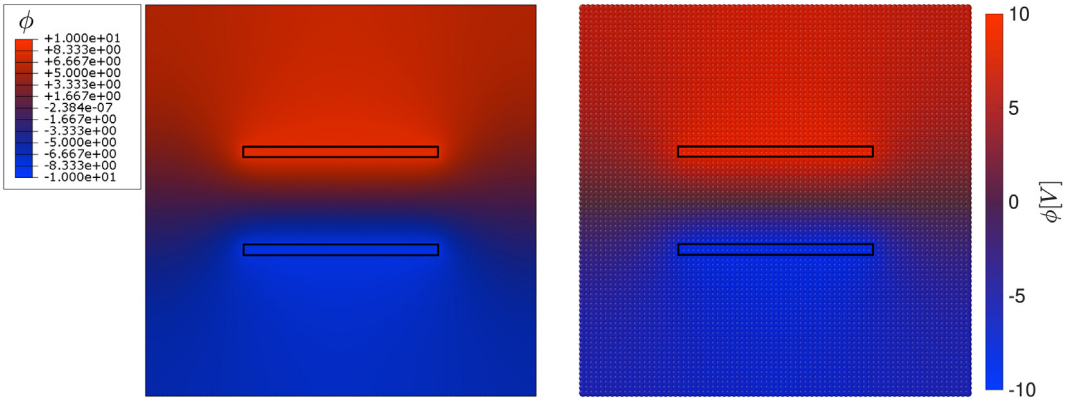

Fig. 10. Square metallic lamina, case (a); Electric potential ϕ calculated using FEM (left) and MPPD (right).

In the second application, two square metallic laminae with different boundary conditions are considered with the geometry in Fig. 9. The laminae, made of Aluminum, have unitary thickness, length $l = 40$ mm and electrical conductivity $K_e = 37\,000$ S/mm. The applied potential difference is $\Delta\phi = 20$ V, whereas the domain is discretized using a regular grid spacing $\Delta x = 0.5$ mm resulting in a model of 6400 particles for the case (a) and 6084 particles for the case (b) (Fig. 9). For the simulations, $m = 3$ is adopted, being commonly used in peridynamics, and representing a good compromise between the accuracy of the local solution and the computational effort [60,62]. The mechanical model has been extensively validated in linear elasticity [18], therefore the attention is here on the electrical part of the model, hence no mechanical boundary conditions are considered. The geometric features of both cases (a) and (b) are chosen to obtain a non-homogeneous electric field, and the results obtained using the present peridynamic formulation are compared with a FE model using ABAQUS [67].[6]

Figs. 10–13 show that the magnitude of the electric current–flux (i.e. the electric current density magnitude $q = J$) and electric field potential ϕ computed using the present formulation, for the two laminae in Fig. 9. The predictions are in excellent agreement with the corresponding FEM solutions. A quantitative comparison of the electric potential predicted by PD and FEM along a central vertical line connecting points d and c (Fig. 9) is shown in Fig. 14. It confirms the accuracy of the proposed formulation and its numerical implementation. A

[6] A regular mesh of 6400 four-nodes elements for coupled thermal-electrical analysis are used for case (a). An irregular mesh of 6152 elements is instead adopted for case (b). Uncoupled electrical analyses are performed by omitting the thermal properties from the material description, in which only the electric potential degrees of freedom are activated in the element and all heat transfer effects are ignored [67].

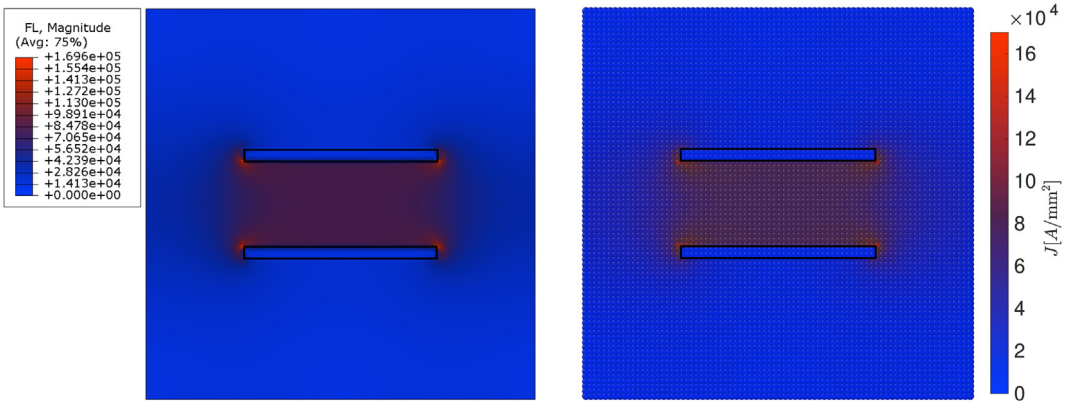

Fig. 11. Square metallic lamina, case (a); Current density J calculated using FEM (left) and MPPD (right).

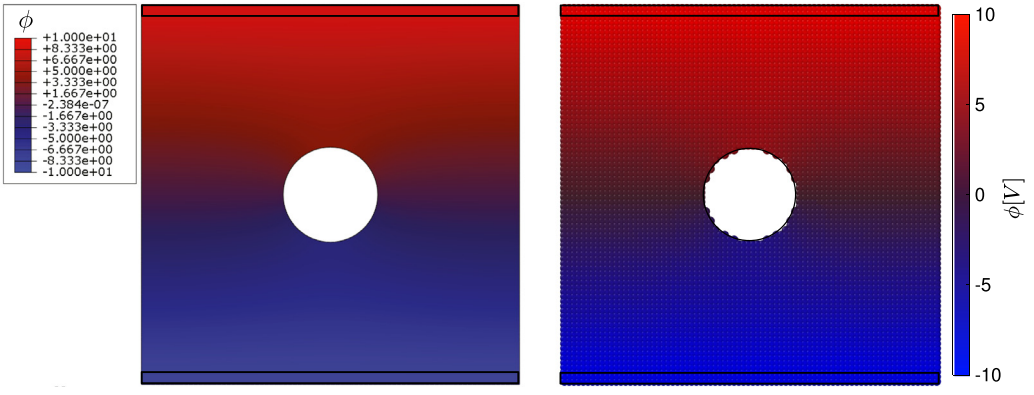

Fig. 12. Square metallic lamina, case (b); Electric potential ϕ calculated using FEM (left) and MPPD (right).

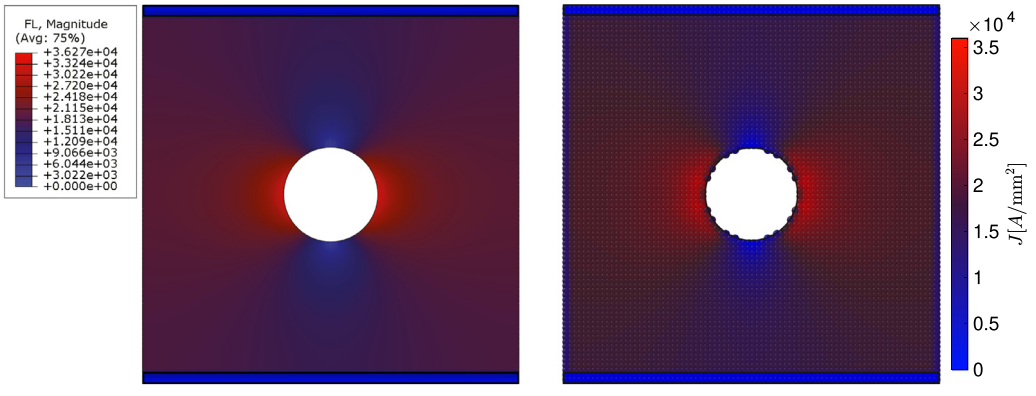

Fig. 13. Square metallic lamina, case (b); Current density J calculated using FEM (left) and MPPD (right).

convergence study (i.e. δ-convergence [68]) has also been performed and the results are summarized in Tables 2–3 and in Fig. 14.

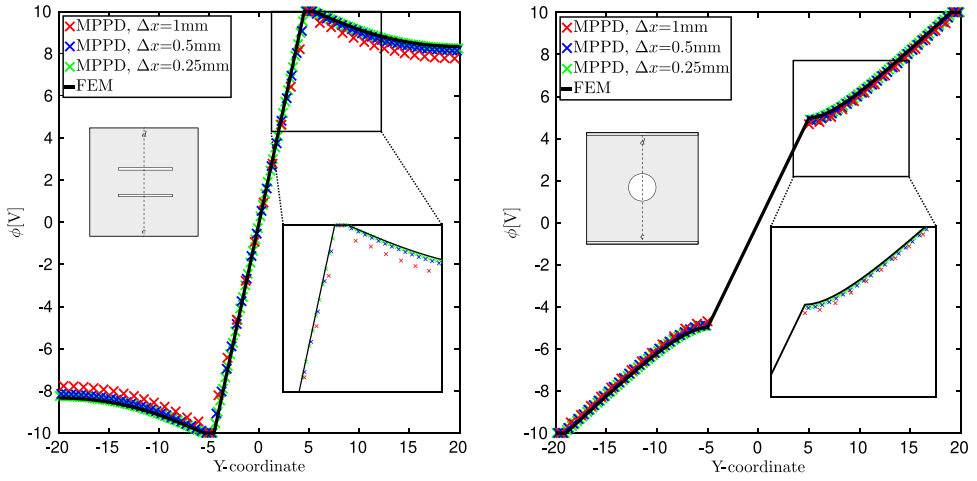

Fig. 14. Square metallic laminae: Comparison of nodal electric field potentials along the central vertical line connecting points d and c, between the FEM solution and peridynamic solutions obtained with $m = 3$ and $\Delta x = 1$ mm, $\Delta x = 0.5$ mm, and $\Delta x = 0.25$ mm.

Table 2
Square laminae, case (a): Discretization adopted and average error in electric potential prediction with respect to FEM solution.

Δx (mm)	δ/l	n. Particles	ϕ: err. (%)
1	0.075	1600	9.44
0.5	0.0125	6400	3.25
0.25	0.00625	25 600	1.87

Table 3
Square laminae, case (b): Discretization adopted and average error in electric potential prediction with respect to FEM solution.

Δx (mm)	δ/l	n. Particles	ϕ: err. (%)
1	0.075	1521	3.91
0.5	0.0125	6084	1.80
0.25	0.00625	24 336	1.04

3.2. Electro-mechanical micropolar damage modeling

A preliminary assessment of the numerical performance of the proposed formulation in the presence of strong discontinuities such as cracks, is detailed as preparation for the validation of the electro-mechanical micropolar damage model. The problem of electrical conduction of a rectangular lamina with an insulated vertical crack has been studied with both peridynamics and FEM. The layout of the problem is shown in Fig. 15, where $a = 400$ mm and $b = 200$ mm, and the assigned length of the crack l is progressively increased from 0 to 0.9 b. The lamina is of unit thickness, electrical conductivity $K_e = 10\,000$ S/mm and an electrical potential difference $\Delta\phi = 2$ V applied to the left and right edges. The discretized model is composed of 3200 particles (regular grid of 80 × 40 particles with $\delta = 0.0375a$). The pre-existing crack is introduced by breaking all of the interactions passing through the crack surfaces at the beginning of the simulation. For each assigned crack length, the electrical field potential is computed with MPPD and FEM, hence the net current I flowing into the lamina is calculated by summing up the electric reactions (concentrated currents) corresponding to the nodes in which the negative electric potential is applied. In this way, applying Ohm's law

$$R = \Delta\phi / I \tag{56}$$

Please cite this article as: V. Diana and V. Carvelli, An electromechanical micropolar peridynamic model, Computer Methods in Applied Mechanics and Engineering (2020) 112998, https://doi.org/10.1016/j.cma.2020.112998.

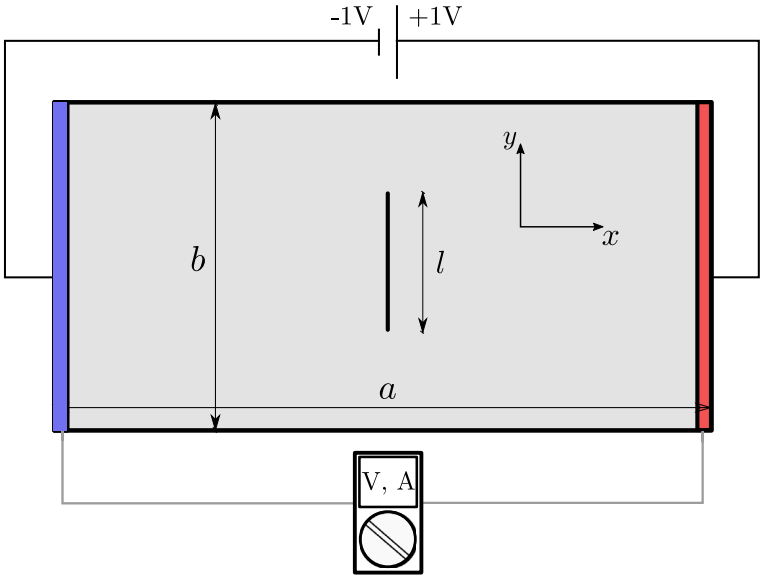

Fig. 15. Electrical conduction in a rectangular lamina with an insulated vertical crack: layout of the problem.

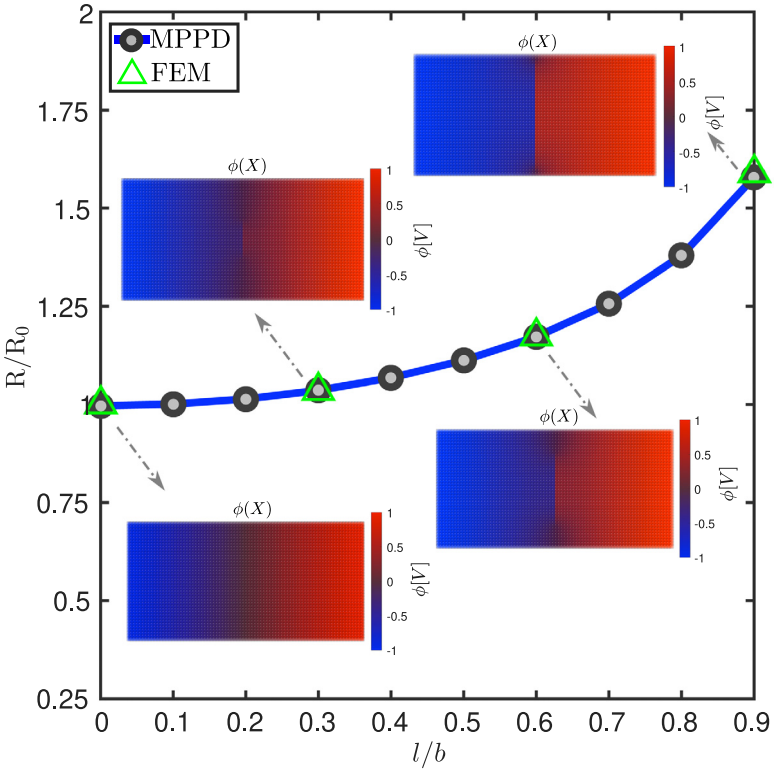

Fig. 16. Variation of the electrical resistance in a rectangular lamina with a vertical crack growth. The electrical resistances are normalized with respect to the resistance R_0 corresponding to the uncracked lamina.

the electrical resistance R is obtained for each crack length considered. Results obtained from peridynamic and FEM analyses are compared in Fig. 16, The latter shows the accuracy of the implicit electrical MPPD model.

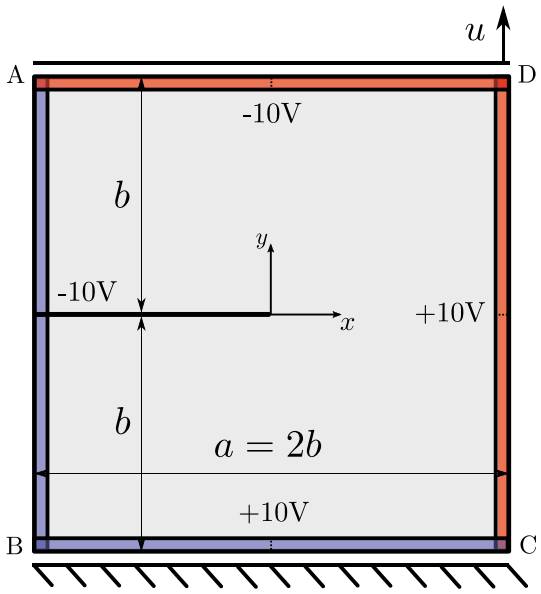

Fig. 17. Single-edge notched specimen tension test: layout of the mechanical and electrical boundary conditions used for damage sensing.

The accuracy of the predicted electrical response allows to study a coupled electro-mechanical problem in which, a pre-existing crack in a square lamina, propagates due to the assigned mechanical loadings (i.e. the assigned displacement field at the top horizontal boundary) and the electrical boundary conditions are used instead for damage sensing (Fig. 17). This is inspired by a well studied problem in phase-field literature [69–71]. It consists of a square plate with unitary thickness, containing a straight horizontal notch of length b located at mid-height of the left vertical edge. The layout of the problem and boundary conditions of the specimen are shown in Fig. 17, where $b = 0.5$ mm. A vertical displacement is applied to all points of the top edge (AD), whereas the bottom edge BC is fixed. Two electric potential differences $\Delta\phi(AB - DC)$ and $\Delta\phi(AD - BC)$ are applied separately to the horizontal edges AB–DC and vertical edges AD–BC, respectively, in order to obtain information on the damage evolution in the plate. In fact, by computing and comparing the reaction currents measured (i.e. the sum of nodes electric concentrated currents I) at A–B and A–D, the corresponding crack growth direction can be estimated. The spatial domain is discretized into 6400 equally spaced particles with $\Delta x = 0.0125$ mm, and the electro-mechanical non-linear simulation is performed under displacement control using a sequentially linear quasi-static procedure with adaptive step refinement [72]. The mechanical and electrical material parameters are: Young's modulus E $= 210$ GPa, Poisson's ratio $\nu = 0$, fracture energy $G_{Ic} = 2.7$ N/mm and electrical conductivity $K_E = 1$ S/mm. The critical stretch is determined instead using Eq. (50). The damage map $d(x)$ and the electric field potential due to $\Delta\phi(AB - DC)$ and $\Delta\phi(AD - BC)$ at various stages of crack propagation are shown in Fig. 18. As the crack propagates, the electric field potential corresponding to $\Delta\phi(AB - DC)$ undergoes important changes, whereas the electric field potential due to $\Delta\phi(AD - BC)$ remains almost the same (see Fig. 18). As a consequence, the electric current due to the potential difference $\Delta\phi(AB - DC)$ remains constant throughout the simulation. On the contrary, the electric current due to the potential difference $\Delta\phi(AB - DC)$ reports a severe drop during the crack propagation process, as Fig. 19 shows. As further validation, the solution of the mechanical problem obtained has also been compared with a Rigid Body-Spring Model (RBSM) solution [55,73] assuming the same pseudo-time step and spatial discretization. The load–displacement curve corresponding to the proposed micropolar peridynamic model is in good agreement with the RBSM solution (Fig. 19).

3.3. A piezoresistive response

The electro-mechanical micropolar peridynamic formulation was also implemented to simulate the piezoresistive behavior of a nanocomposite material. In particular, the material under consideration is a polyvinyl alcohol (PVA)

Please cite this article as: V. Diana and V. Carvelli, An electromechanical micropolar peridynamic model, Computer Methods in Applied Mechanics and Engineering (2020) 112998, https://doi.org/10.1016/j.cma.2020.112998.

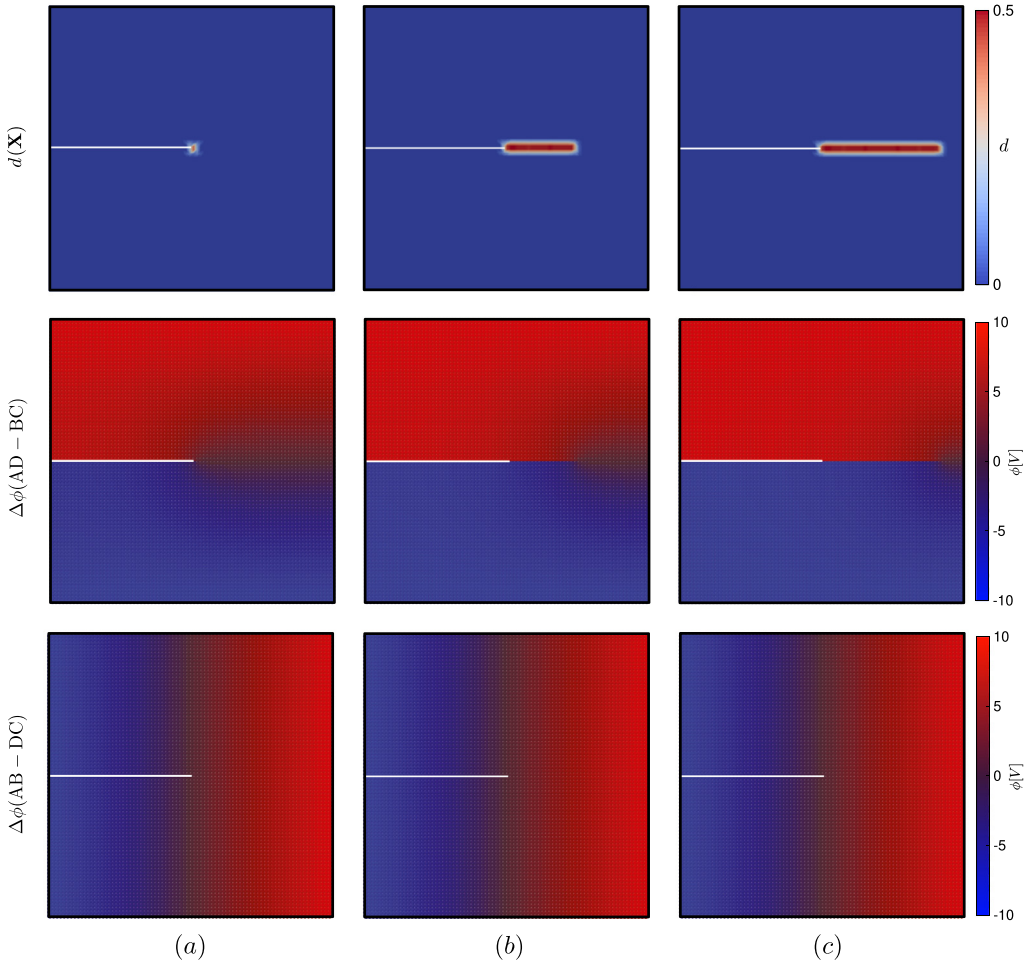

Fig. 18. Single-edge notched specimen tension test: Damage map and electric field potential due to $\Delta\phi(AB-DC)$ and $\Delta\phi(AD-BC)$ at displacements (a) u $= 6.98 \times 10^{-3}$ mm, (b) u $= 7.04 \times 10^{-3}$ mm, (c) u $= 7.08 \times 10^{-3}$ mm.

infiltrated multi-walled carbon nanotube (MWCNTs) buckypaper (BP) for strain sensing application [74]. These types of nanocomposites are fabricated by a sequence of vacuum filtration and polymer intercalation technique and due to their specific electro-mechanical properties they are suitable in a wide range of applications, ranging from automotive components to medical devices [74]. The experimental data adopted for comparison, are detailed in [74], in which the authors studied the elecro-mechanical behavior of MWCNTs BP/PVA composites characterized by different MWCNTs contents (50 wt%, 65 wt% and 80 wt%). A MWCNTs BP (100 wt%) was also considered for comparison purposes. Uniaxial tensile tests were performed [74] to evaluate the potentialities of the BP/PVA composite as a strain sensor. For the study of piezoresistivity effect, several BP samples, whose geometric features are shown in Fig. 20, and infiltrated with different amount of PVA solution were fabricated. The main electromechanical properties of MWCNTs BP/PVA samples with different MWCNTs contents were evaluated in the elastic range (up to $\varepsilon = 2.0\%$), and are summarized in Table 4 and Fig. 21, where the electrical conductivities and resistivities of the composites, measured using a two-point probe method, are referred to the unstretched samples. The relative resistance changes of all samples were found to increase linearly with the strain applied. The increment

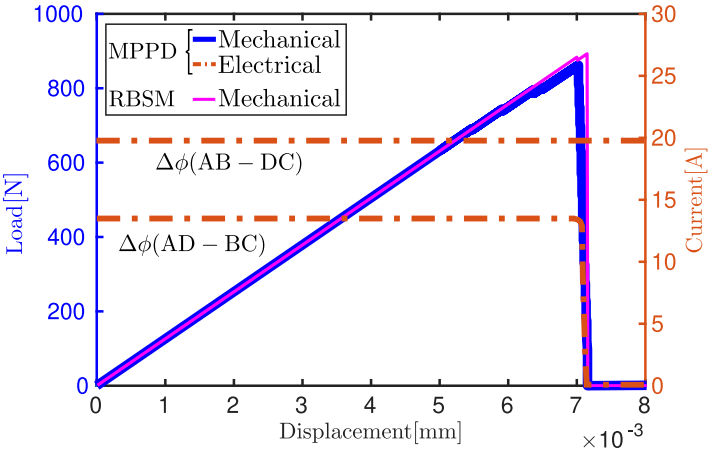

Fig. 19. Single-edge notched specimen tension test: Load–displacement and electric current–displacement curves. Comparison between mechanical response predicted by MPPD and RBSM.

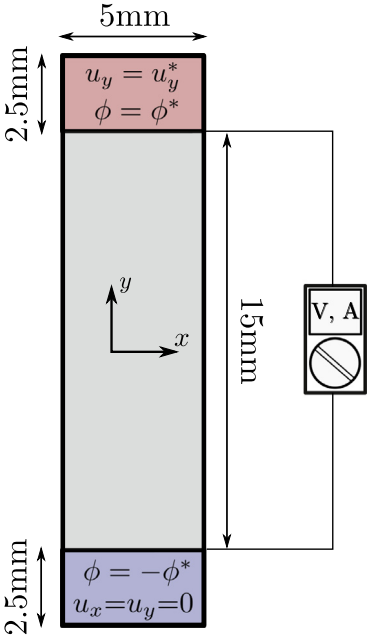

Fig. 20. Layout of the uniaxial tensile test performed on MWCNTs BP/PVA samples.

of resistance with strain can be attributed to the reduction of the conductive MWCNTs network density and the increase of inter-tube distances induced by tensile strains [74]. For further details please refer to [74]. By considering Eq. (56) and

$$R = \rho_e \frac{l}{A}; \qquad \rho_e = \frac{1}{K_e} \tag{57}$$

where ρ_e is the electrical resistivity, l the gauge length and A the cross-sectional area, it is possible to determine the values of the electrical conductivity K_e of the samples associated to each value of strain ε (i.e. ε_{yy}) during the tensile test. In particular the following linear relationship between the actual electrical resistivity ρ_e and the strain ε_{yy}, can be derived from the experimental data

$$\rho_e = \rho_{e_0} + \alpha_{\rho_e} \varepsilon_{yy} \tag{58}$$

Please cite this article as: V. Diana and V. Carvelli, An electromechanical micropolar peridynamic model, Computer Methods in Applied Mechanics and Engineering (2020) 112998, https://doi.org/10.1016/j.cma.2020.112998.

Table 4
Summary of the electromechanical properties of MWCNTs BP/PVA samples with different MWCNTs content. The electrical conductivity is referred to the unstretched samples [74].

Sample name	Young's Modulus, E (GPa)	Thickness, t (mm)	Electrical conductivity, K_{e_0} (S/m)
100-BP	1.39	0.50	1.03×10^3
80-BP/PVA	2.91	0.63	4.07×10^2
65-BP/PVA	4.02	0.65	2.35×10^2
50-BP/PVA	3.43	0.68	1.07×10^2

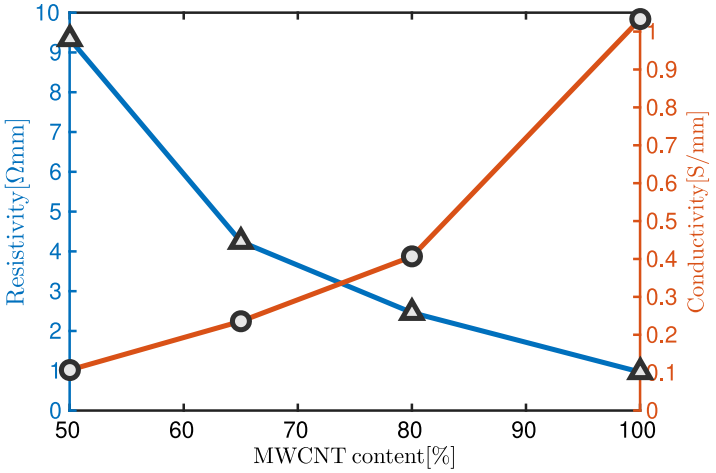

Fig. 21. Electrical resistivity and conductivity of unstretched MWCNTs BP/PVA samples as a function of MWCNTs content in the composites [74].

where ρ_{e_0} is the electrical resistivity of the unstretched samples, and α_{ρ_e} is a parameter (same dimension of the electrical resistivity) getting the value 0.726 Ω mm, 4.689 Ω mm, 11.050 Ω mm and 27.322 Ω mm for 100-BP, 80-BP/PVA, 65-BP/PVA and 50-BP/PVA specimen, respectively.

Hence, numerical simulations of those tensile tests are performed using the present peridynamic electromechanical formulation. The specimens are discretized into 2500 particles equally-spaced, with $\Delta x = 0.2$ mm and $m = 3$, and the boundary conditions are described in Fig. 20. The electrical conductivity of a particle is updated based on the actual value of strain at that material particle. As non-linear quasi-static scheme in displacement control [72] is adopted, and since the specimen is subjected to a homogeneous deformation field, at each step of the simulation the value of ε_{yy} corresponding to the applied displacement field is known. Thus, the homogeneous actual peridynamic microelectrical constants k_e are calculated for each material considered and for each value of the applied displacement with Eqs. (57), (58) and (40).

Remark 3. The applied strain could lead to an anisotropic piezoresistive response in nanocomposites [75–77]. However, by using the data from the uniaxial tensile test performed by Yee et al. [74] we have information regarding the relationship between the conductivity $K_{e_{yy}}$ and the strain ε_{yy}, while no information on the behavior in the transversal direction (relationship between $K_{e_{xx}}$ and ε_{xx}) are deductible. Hence, an isotropic piezoresistive behavior is considered in the simulations, and thus the peridynamic microelectrical constant k_e is assumed to be independent of the bond orientation angle ψ.

Remark 4. In the general case of non-homogeneous deformation field, the computation of the strain tensor at each particle's position and at each step of the simulation could be necessary to properly describe the piezoresistive response of a certain material. The electrical conductivity of a specific bond would be then calculated as the average of the conductivities corresponding to the two particles connected by that bond. A possible simple strategy for

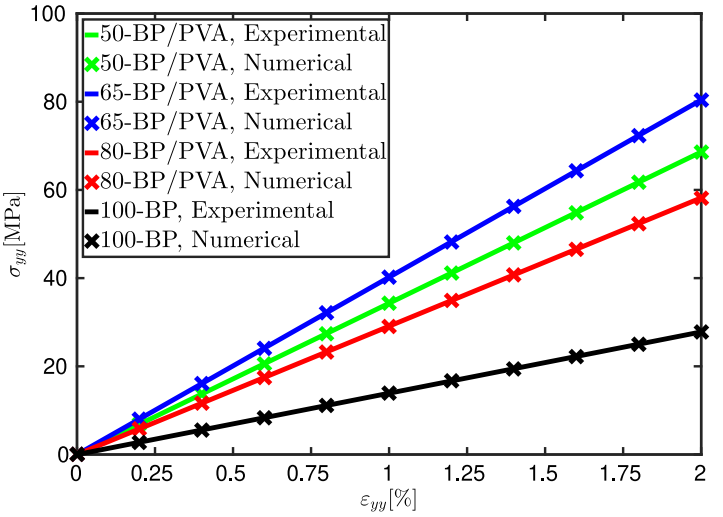

Fig. 22. Experimental and numerical uniaxial tensile stress–strain curves of the MWCNTs BP/PVA composites.

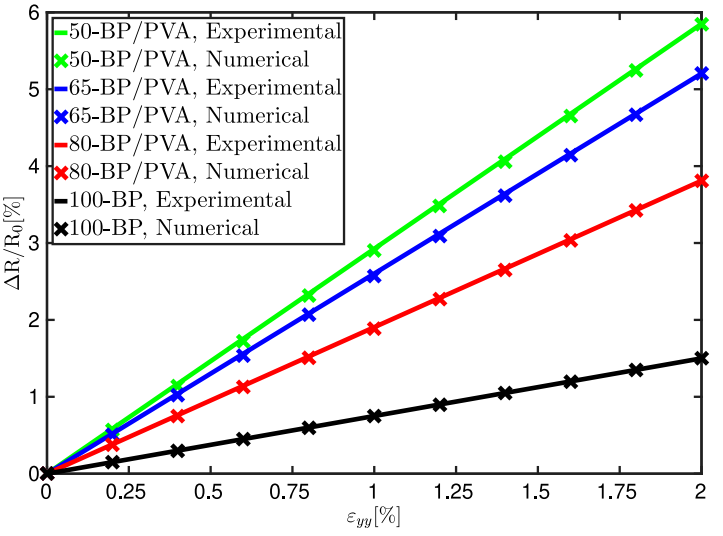

Fig. 23. Experimental and numerical relative resistance variation as a function of mechanical strain of MWCNTs BP/PVA composites.

computing the strain at a particle is to follow the approach suggested by Prakash and Seidel [6], based on non-local shape tensors, commonly used in state-based peridynamics. Using basic kinematics, the infinitesimal strains can then be obtained from the deformation gradient [6]. It is worth noting that while bond-based peridynamic models are being used, the evaluation of volume averaged field quantities in post processing steps is facilitated by use of non-local gradients from the state based theory so as to have an unambiguous notion of the gradients of primary field variables [6]. Since linearized bond based models have shown to be a particular case of the more general state based models [63], this approach could be used to correctly estimate fields while reducing computational effort [6]. For further details refers to [6].

As described in the previous subsection, the electrical resistance R at each step of the simulation and for each material considered, is determined by computing the actual net current I flowing into the specimens, and then applying Eq. (56). The results from the electromechanical simulation are in perfect agreement with the experimental data, as Figs. 22 and 23 show. It is worth nothing that, despite the electrical resistances R (i.e. $\Delta R/R_0$) of the

specimens vary linearly with the deformation ε_{yy} as in the case of non piezoresistive materials, the material behavior is non-linear since the electrical conductivities K_e are function of the deformation as well. Hence, the slopes of the curves in Fig. 23 are different to those of non piezoresistive materials with the mechanical properties in Table 4 and constant electrical conductivity K_{E_0}. In this case, the change of resistance with the deformation would be only caused by a geometric effect due to change in dimensions of the specimens, according to the well known

$$R = \frac{l}{K_{e_0} A} \tag{59}$$

4. Conclusions

In this paper an analytical implicit peridynamic formulation for in-plane electro-mechanical problems has been proposed. By defining a proper microelectrical energy function and a specific electrical inelastic deformation parameter, the constitutive equation and the compatibility conditions have been imposed, and the expression of the electrical stiffness operator has been derived. The electrical peridynamic model is then coupled with a mechanical micropolar formulation capable to handle variable Poisson's ratios and non-homogeneous deformation fields in isotropic Cauchy solids. In this way, a unified stiffness operator and thus an implicit micropolar peridynamic electro-mechanical formulation has been obtained. Moreover a damage model for brittle electrically conductive materials has been proposed.

The electromechanical peridynamic formulation, that has been validated by Analytical solutions, FE solutions and experimental results, demonstrated its capabilities in predicting the electric field potential and current density in electrical and electro-mechanical problems involving fracture and piezoresistive response. Further studies and experimental data are needed to extend the present formulation to anisotropic conductive materials.

Declaration of competing interest

The authors declare that they have no known competing financial interests or personal relationships that could have appeared to influence the work reported in this paper.

Acknowledgments

The authors gratefully acknowledge Prof. Siro Casolo, for the fruitful discussions. Moreover they wish to express their gratitude to Vito Tateo for the calculations made using the original RBSM code developed by the Casolo's team at Politecnico di Milano, Italy.

Appendix. Strain energy and macroelastic energy densities

The microelastic energy function in isotropic micropolar peridynamics is described by Eq. (24) considering that for homogeneous deformation fields the particles rotations $\theta = 0$

$$\begin{aligned}\Phi(\mathbf{X}) &= \frac{1}{2}\int_{H_x} \frac{k_n s^2|\boldsymbol{\xi}|}{2} + \frac{k_t \gamma^2|\boldsymbol{\xi}|}{2} + \frac{k_\theta \vartheta^2}{2} dV_{\mathbf{X}'} \\ &= \frac{1}{2}\int_{H_x} \frac{k_n s^2|\boldsymbol{\xi}|}{2} + \frac{k_t \gamma^2|\boldsymbol{\xi}|}{2} dV_{\mathbf{X}'}\end{aligned} \tag{A.1}$$

The deformation variables s and γ of each bond in Eq. (A.1) are in general functions of the angle of inclination ψ of the ligament. However, in the case of isotropic expansion, we can write

$$s = s; \qquad \gamma = 0 \tag{A.2}$$

From Eq. (A.1), we obtain

$$\begin{aligned}\Phi(\mathbf{X}) &= \frac{1}{2}\int_{H_x} \frac{k_n s^2|\boldsymbol{\xi}|}{2} dV_{\mathbf{X}'} = \frac{1}{2}\int_{H_x} \frac{k_n \mathrm{t} s^2|\boldsymbol{\xi}|}{2} dA_{\mathbf{X}'} \\ &= \frac{1}{2}\int_0^\delta \frac{2k_n \mathrm{t}\pi s^2|\boldsymbol{\xi}|^2}{2} d\xi = \frac{k_n \mathrm{t}\pi s^2 \delta^3}{6}\end{aligned} \tag{A.3}$$

where t is the thickness. In conventional continuum mechanics, for elastic solids under isotropic expansion, the linear elastic strain energy density function for plane stress can be written as

$$\frac{1}{2}C_{ij}\epsilon_i\epsilon_j = \frac{E}{2(1-\nu^2)}\begin{bmatrix} 1 & \nu & 0 \\ \nu & 1 & 0 \\ 0 & 0 & \frac{1-\nu}{2} \end{bmatrix}\begin{Bmatrix} s \\ s \\ 0 \end{Bmatrix}\cdot\begin{Bmatrix} s \\ s \\ 0 \end{Bmatrix} = \frac{Es^2}{1-\nu} \tag{A.4}$$

and for plane strain as

$$\frac{1}{2}C_{ij}\epsilon_i\epsilon_j = \frac{E}{2(1-2\nu)(1+\nu)}\begin{bmatrix} 1-\nu & \nu & 0 \\ \nu & 1-\nu & 0 \\ 0 & 0 & \frac{1-2\nu}{2} \end{bmatrix}\begin{Bmatrix} s \\ s \\ 0 \end{Bmatrix}\cdot\begin{Bmatrix} s \\ s \\ 0 \end{Bmatrix} = \frac{Es^2}{(1-2\nu)(1+\nu)} \tag{A.5}$$

In the case of pure shear deformation, instead, s and γ in Eq. (A.1) are functions of the angle ψ according to

$$s = s\cos(2\psi); \qquad \gamma = \gamma\sin(2\psi) \tag{A.6}$$

so that

$$\begin{aligned} \Phi(\mathbf{X}) &= \frac{1}{2}\int_{H_x}\frac{k_n s^2\cos^2(2\psi)|\boldsymbol{\xi}|}{2} + \frac{k_t\gamma^2\sin^2|\boldsymbol{\xi}|(2\psi)}{2}dV_{\mathbf{X}'} \\ &= \frac{1}{2}\int_{H_x}\frac{k_n \mathrm{t} s^2\cos^2(2\psi)|\boldsymbol{\xi}|}{2} + \frac{k_t \mathrm{t}\gamma^2\sin^2|\boldsymbol{\xi}|(2\psi)}{2}dA_{\mathbf{X}'} \\ &= \frac{1}{2}\int_0^{\delta} 4\int_0^{\pi/2}\frac{k_n \mathrm{t} s^2\cos^2(2\psi)|\boldsymbol{\xi}|}{2} + \frac{k_t \mathrm{t}\gamma^2\sin^2(2\psi)|\boldsymbol{\xi}|}{2}d\psi\, d\xi \\ &= \int_0^{\delta}\frac{k_n \mathrm{t} s^2\,[4\psi+\sin(4\psi)]|\boldsymbol{\xi}|^2}{8} + \frac{k_t \mathrm{t}\gamma^2\,[4\psi-\sin(4\psi)]|\boldsymbol{\xi}|^2}{8}\Bigg|_0^{\pi/2}d\xi \\ &= \frac{k_n \mathrm{t}\pi s^2\delta^3}{12} + \frac{k_t \mathrm{t}\pi\gamma^2\delta^3}{24} \end{aligned} \tag{A.7}$$

The conventional linear elastic strain energy density function for plane stress conditions is obtained by

$$\frac{1}{2}C_{ij}\epsilon_i\epsilon_j = \frac{E}{2(1-\nu^2)}\begin{bmatrix} 1 & \nu & 0 \\ \nu & 1 & 0 \\ 0 & 0 & \frac{1-\nu}{2} \end{bmatrix}\begin{Bmatrix} s \\ -s \\ 0 \end{Bmatrix}\cdot\begin{Bmatrix} s \\ -s \\ 0 \end{Bmatrix} = \frac{Es^2}{1+\nu} \tag{A.8}$$

and for plane strain, by

$$\frac{1}{2}C_{ij}\epsilon_i\epsilon_j = \frac{E}{2(1-2\nu)(1+\nu)}\begin{bmatrix} 1-\nu & \nu & 0 \\ \nu & 1-\nu & 0 \\ 0 & 0 & \frac{1-2\nu}{2} \end{bmatrix}\begin{Bmatrix} s \\ -s \\ 0 \end{Bmatrix}\cdot\begin{Bmatrix} s \\ -s \\ 0 \end{Bmatrix} = \frac{Es^2}{1+\nu} \tag{A.9}$$

References

[1] S. Silling, Reformulation of elasticity theory for discontinuities and long-range forces, J. Mech. Phys. Solids 48 (1) (2000) 175–209.
[2] E. Madenci, E. Oterkus, Peridynamic Theory and Its Applications, Springer Science, New York, 2014,
[3] A. Eringen, D. Edelen, On nonlocal elasticity, Internat. J. Engrg. Sci. 10 (3) (1972) 233–248.
[4] C. Polizzotto, Nonlocal elasticity and related variational principles, Int. J. Solids Struct. 38 (42–43) (2001) 7359–7380.
[5] S. Silling, R. Lehoucq, Convergence of peridynamics to classical elasticity theory, J. Elasticity 93 (1) (2008) 13–37.
[6] N. Prakash, G.D. Seidel, Electromechanical peridynamics modeling of piezoresistive response of carbon nanotube nanocomposites, Comput. Mater. Sci. 113 (2016) 154–170.
[7] C. Navier, Mémoire sur les lois de l'équilibre et du mouvement des corps solides élastiques, in: Mémoire lu a l'Académie royale des sciences, Vol. 6, 1827, pp. 375–384.
[8] A. Cauchy, Mémoire sur les systèmes isotropes de points matériels, Mém. Acad. Sci. t. XXII (1850) 351–386.
[9] S.D. Poisson, Mémoire sur les équations générales de l'équilibre et le du mouvement des corps solides élastiques et des fluides, J. l'École Polytech. 13 (20) (1831) 1–174.
[10] S. Silling, M. Epton, O. Weckner, J. Xu, E. Askari, Peridynamic states and constitutive modeling, J. Elasticity 88 (2) (2007) 151–184.
[11] T.L. Warren, S.A. Silling, A. Askari, O. Weckner, M.A. Epton, J. Xu, A non-ordinary state-based peridynamic method to model solid material deformation and fracture, Int. J. Solids Struct. 46 (5) (2009) 1186–1195.
[12] P. Li, Z. Hao, W. Zhen, A stabilized non-ordinary state-based peridynamic model, Comput. Methods Appl. Mech. Engrg. 339 (2018) 262–280.

Please cite this article as: V. Diana and V. Carvelli, An electromechanical micropolar peridynamic model, Computer Methods in Applied Mechanics and Engineering (2020) 112998, https://doi.org/10.1016/j.cma.2020.112998.

[13] Y. Wang, X. Zhou, Y. Wang, Y. Shou, A 3-D conjugated bond-pair-based peridynamic formulation for initiation and propagation of cracks in brittle solids, Int. J. Solids Struct. 134 (2018) 89–115.
[14] Y. Wang, X. Zhou, Y. Shou, The modeling of crack propagation and coalescence in rocks under uniaxial compression using the novel conjugated bond-based peridynamics, Int. J. Mech. Sci. 128–129 (2017) 614–643.
[15] W. Gerstle, N. Sau, S. Silling, Peridynamic modeling of concrete structures, Nucl. Eng. Des. 237 (12) (2007) 1250–1258.
[16] W. Gerstle, Introduction to Practical Peridynamics: Computational Solid Mechanics Without Stress and Strain, World Scientific Publishing Co. Pte. Ltd., 2016.
[17] W. Voigt, Lehrbuch der Kristallphysik, 1928.
[18] V. Diana, S. Casolo, A bond-based micropolar peridynamic model with shear deformability: Elasticity, failure properties and initial yield domains, Int. J. Solids Struct. 160 (2019) 201–231.
[19] V. Diana, S. Casolo, A full orthotropic micropolar peridynamic formulation for linearly elastic solids, Int. J. Mech. Sci. 160 (2019) 140–155.
[20] F. Bobaru, Y. Ha, W. Hu, Damage progression from impact in layered glass modeled with peridynamics, Cent. Eur. J. Eng. 2 (4) (2012) 551–561.
[21] S. Casolo, V. Diana, Modelling laminated glass beam failure via stochastic rigid body-spring model and bond-based peridynamics, Eng. Fract. Mech. 190 (2018) 331–346.
[22] A. Shojaei, F. Mossaiby, M. Zaccariotto, U. Galvanetto, An adaptive multi-grid peridynamic method for dynamic fracture analysis, Int. J. Mech. Sci. 144 (2018) 600–617.
[23] P. Roy, A. Pathrikar, S. Deepu, D. Roy, Peridynamics damage model through phase field theory, Int. J. Mech. Sci. 128–129 (2017) 181–193.
[24] E. Madenci, S. Oterkus, Ordinary state-based peridynamics for plastic deformation according to von Mises yield criteria with isotropic hardening, J. Mech. Phys. Solids 86 (2016) 192–219.
[25] M.M. Rahaman, P. Roy, D. Roy, J. Reddy, A peridynamic model for plasticity: Micro-inertia based flow rule, entropy equivalence and localization residuals, Comput. Methods Appl. Mech. Engrg. 327 (2017) 369–391.
[26] O. Weckner, N.A.N. Mohamed, Viscoelastic material models in peridynamics, Appl. Math. Comput. 219 (11) (2013) 6039–6043.
[27] A. Pathrikar, M.M. Rahaman, D. Roy, A thermodynamically consistent peridynamics model for visco-plasticity and damage, Comput. Methods Appl. Mech. Engrg. 348 (2019) 29–63.
[28] W. Gerstle, S. Silling, D. Read, V. Tewary, R. Lehoucq, Peridynamic simulation of electromigration, Tech. Sci. Press 8 (2) (2008) 75–92.
[29] F. Bobaru, M. Duangpanya, The peridynamic formulation for transient heat conduction, Int. J. Heat Mass Transfer 53 (19) (2010) 4047–4059.
[30] F. Bobaru, M. Duangpanya, A peridynamic formulation for transient heat conduction in bodies with evolving discontinuities, J. Comput. Phys. 231 (7) (2012) 2764–2785.
[31] S. Oterkus, E. Madenci, A. Agwai, Peridynamic thermal diffusion, J. Comput. Phys. 265 (2014) 71–96.
[32] S. Oterkus, E. Madenci, A. Agwai, Fully coupled peridynamic thermomechanics, J. Mech. Phys. Solids 64 (2014) 1–23.
[33] S. Bazazzadeh, F. Mossaiby, A. Shojaei, An adaptive thermo-mechanical peridynamic model for fracture analysis in ceramics, Eng. Fract. Mech. 223 (2020) 106708.
[34] P. D'Antuono, M. Morandini, Thermal shock response via weakly coupled peridynamic thermo-mechanics, Int. J. Solids Struct. 129 (2017) 74–89.
[35] S. Oterkus, J. Fox, E. Madenci, Simulation of electro-migration through peridynamics, in: 2013 IEEE 63rd Electronic Components and Technology Conference, 2013, pp. 1488–1493.
[36] Z. Chen, F. Bobaru, Peridynamic modeling of pitting corrosion damage, J. Mech. Phys. Solids 78 (2015) 352–381.
[37] Y. Zhang, G. Pan, Y. Zhang, S. Haeri, A multi-physics peridynamics-DEM-IB-CLBM framework for the prediction of erosive impact of solid particles in viscous fluids, Comput. Methods Appl. Mech. Engrg. 352 (2019) 675–690.
[38] N. Prakash, G.D. Seidel, Computational electromechanical peridynamics modeling of strain and damage sensing in nanocomposite bonded explosive materials (NCBX), Eng. Fract. Mech. 177 (2017) 180–202.
[39] N. Prakash, G.D. Seidel, Effects of microscale damage evolution on piezoresistive sensing in nanocomposite bonded explosives under dynamic loading via electromechanical peridynamics, Modelling Simulation Mater. Sci. Eng. 26 (1) (2017) 015003.
[40] L. Gao, E.T. Thostenson, Z. Zhang, T.-W. Chou, Coupled carbon nanotube network and acoustic emission monitoring for sensing of damage development in composites, Carbon 47 (5) (2009) 1381–1388.
[41] J.J. Ku-Herrera, F. Avilés, G.D. Seidel, Self-sensing of elastic strain, matrix yielding and plasticity in multiwall carbon nanotube/vinyl ester composites, Smart Mater. Struct. 22 (8) (2013) 085003.
[42] F. Bobaru, J. Foster, P. Geubelle, S. Silling, Handbook of Peridynamic Modeling, in: Advances in Applied Mathematics, CRC Press, 2015.
[43] V. Diana, Discrete Physically-Based Models in Solid Mechanics (Ph.D. dissertation), Politecnico di Milano, Milano, Italy, 2019.
[44] W. Gerstle, N. Sau, N. Sakhavand, On Peridynamic Computational Simulation of Concrete Structures, No. 265 SP, American Concrete Institute, ACI Special Publication, 2009, pp. 245–264.
[45] W. Liu, J.-W. Hong, Discretized peridynamics for linear elastic solids, Comput. Mech. 50 (5) (2012) 579–590.
[46] Q.V. Le, F. Bobaru, Surface corrections for peridynamic models in elasticity and fracture, Comput. Mech. (2017).
[47] W. Voigt, Theoretische Studien über die Elasticitätsverhältnisse der Krystalle, Abh. Ges. Wiss. Gottingen 34 (1887) 3–51.
[48] Z. Pan, R. Ma, D. Wang, A. Chen, A review of lattice type model in fracture mechanics: theory, applications, and perspectives, Eng. Fract. Mech. 190 (2018) 382–409.

Please cite this article as: V. Diana and V. Carvelli, An electromechanical micropolar peridynamic model, Computer Methods in Applied Mechanics and Engineering (2020) 112998, https://doi.org/10.1016/j.cma.2020.112998.

[49] H. Ren, X. Zhuang, T. Rabczuk, A new peridynamic formulation with shear deformation for elastic solid, J. Micromech. Mol. Phys. 01 (02) (2016) 1650009.
[50] G.F. Zhao, J. Fang, J. Zhao, A 3D distinct lattice spring model for elasticity and dynamic failure 35 (8), 2011, pp. 859–885.
[51] W.-J. Li, Q.-Z. Zhu, T. Ni, A local strain-based implementation strategy for the extended peridynamic model with bond rotation, Comput. Methods Appl. Mech. Engrg. 358 (2020) 112625.
[52] I. Stakgold, The cauchy relations in a molecular theory of elasticity, Quart. Appl. Math. 8 (2) (1950) 169–186.
[53] M. Ostoja-Starzewski, Lattice models in micromechanics, Appl. Mech. Rev. 55 (1) (2002) 35–59.
[54] S. Casolo, Macroscopic modelling of structured materials: Relationship between orthotropic Cosserat continuum and rigid elements, Int. J. Solids Struct. 43 (3–4) (2006) 475–496.
[55] S. Casolo, Macroscale modelling of microstructure damage evolution by a rigid body and spring model, J. Mech. Mater. Struct. 4 (3) (2009) 551–570.
[56] R. Lehoucq, S. Silling, Force flux and the peridynamic stress tensor, J. Mech. Phys. Solids 56 (4) (2008) 1566–1577.
[57] A.B.d. Saint Venant, Note sur la pression dans l'intérieur des corps ou à leurs surfaces de séparation, C. R. Acad. Sci. 1 (1845) 24–26.
[58] S. Timoshenko, History of Strength of Materials, Dover, New York, 1983.
[59] M. Breitenfeld, P. Geubelle, O. Weckner, S. Silling, Non-ordinary state-based peridynamic analysis of stationary crack problems, Comput. Methods Appl. Mech. Engrg. 272 (2014) 233–250.
[60] R. Ballarini, V. Diana, L. Biolzi, S. Casolo, Bond-based peridynamic modelling of singular and nonsingular crack-tip fields, Meccanica 53 (14) (2018) 3495–3515.
[61] Z. Chen, F. Bobaru, Selecting the kernel in a peridynamic formulation: A study for transient heat diffusion, Comput. Phys. Comm. 197 (2015) 51–60.
[62] S. Silling, E. Askari, A meshfree method based on the peridynamic model of solid mechanics, Comput. Struct. 83 (17–18) (2005) 1526–1535.
[63] S. Silling, R. Lehoucq, Peridynamic theory of solid mechanics, Adv. Appl. Mech. 44 (2010) 73–168.
[64] R. Panchadhara, P.A. Gordon, Application of peridynamic stress intensity factors to dynamic fracture initiation and propagation, Int. J. Fract. 201 (1) (2016) 81–96.
[65] D. Dipasquale, M. Zaccariotto, U. Galvanetto, Crack propagation with adaptive grid refinement in 2D peridynamics, Int. J. Fract. 190 (1) (2014) 1–22.
[66] C. Jiang, G.-F. Zhao, N. Khalili, On crack propagation in brittle material using the distinct lattice spring model, Int. J. Solids Struct. 118–119 (2017) 41–57.
[67] ABAQUS/Standard User's Manual, Simulia, 2016.
[68] F. Bobaru, Peridynamics and multiscale modeling, Int. J. Multiscale Comput. Eng. 9 (6) (2011) vii–ix.
[69] C. Miehe, M. Hofacker, F. Welschinger, A phase field model for rate-independent crack propagation: Robust algorithmic implementation based on operator splits, Comput. Methods Appl. Mech. Engrg. 199 (45) (2010) 2765–2778.
[70] J. Kiendl, M. Ambati, L.D. Lorenzis, H. Gomez, A. Reali, Phase-field description of brittle fracture in plates and shells, Comput. Methods Appl. Mech. Engrg. 312 (2016) 374–394.
[71] R. Patil, B. Mishra, I. Singh, An adaptive multiscale phase field method for brittle fracture, Comput. Methods Appl. Mech. Engrg. 329 (2018) 254–288.
[72] T. Ni, M. Zaccariotto, Q.-Z. Zhu, U. Galvanetto, Static solution of crack propagation problems in peridynamics, Comput. Methods Appl. Mech. Engrg. 346 (2019) 126–151.
[73] S. Casolo, Modelling in-plane micro-structure of masonry walls by rigid elements, Int. J. Solids Struct. 41 (13) (2004) 3625–3641.
[74] M. Yee, N. Mubarak, M. Khalid, E. Abdullah, P. Jagadish, Synthesis of polyvinyl alcohol (PVA) infiltrated MWCNTs buckypaper for strain sensing application, Sci. Rep., Nat. Publ. Group 8 (1) (2018) 17295.
[75] C. Grimaldi, P. Ryser, S. Strssler, Piezoresistive anisotropy of thick-film resistors, J. Eur. Ceram. Soc. 24 (6) (2004) 1893–1896.
[76] H. Lee, D. Kwon, H. Cho, I. Park, J. Kim, Soft Nanocomposite Based Multi-point, Multi-directional Strain Mapping Sensor Using Anisotropic Electrical Impedance Tomography, Vol. 7, Scientific Reports, Nature Publishing Group, 2017.
[77] C.-W. Jiang, I.-C. Ni, S.-D. Tzeng, W. Kuo, Nearly Isotropic Piezoresistive Response Due to Charge Detour Conduction in Nanoparticle Thin Films, Vol. 5, Scientific Reports, Nature Publishing Group, 2015.

Please cite this article as: V. Diana and V. Carvelli, An electromechanical micropolar peridynamic model, Computer Methods in Applied Mechanics and Engineering (2020) 112998, https://doi.org/10.1016/j.cma.2020.112998.